

MULTI-FIDELITY PARAMETER ESTIMATION USING CONDITIONAL DIFFUSION MODELS

CAROLINE TATSUOKA[†], MINGLEI YANG[‡], DONGBIN XIU[†], AND GUANNAN ZHANG[§]

Abstract. We present a multi-fidelity method for uncertainty quantification of parameter estimates in complex systems, leveraging generative models trained to sample the target conditional distribution. In the Bayesian inference setting, traditional parameter estimation methods rely on repeated simulations of potentially expensive forward models to determine the posterior distribution of the parameter values, which may result in computationally intractable workflows. Furthermore, methods such as Markov Chain Monte Carlo (MCMC) necessitate rerunning the entire algorithm for each new data observation, further increasing the computational burden. Hence, we propose a novel method for efficiently obtaining posterior distributions of parameter estimates for high-fidelity models given data observations of interest. The method first constructs a low-fidelity, conditional generative model capable of amortized Bayesian inference and hence rapid posterior density approximation over a wide-range of data observations. When higher accuracy is needed for a specific data observation, the method employs adaptive refinement of the density approximation. It uses outputs from the low-fidelity generative model to refine the parameter sampling space, ensuring efficient use of the computationally expensive high-fidelity solver. Subsequently, a high-fidelity, unconditional generative model is trained to achieve greater accuracy in the target posterior distribution. Both low- and high- fidelity generative models enable efficient sampling from the target posterior and do not require repeated simulation of the high-fidelity forward model. We demonstrate the effectiveness of the proposed method on several numerical examples, including cases with multi-modal densities, as well as an application in plasma physics for a runaway electron simulation model.

Key words. Parameter estimation, uncertainty quantification, score-based diffusion models, density estimation, multi-fidelity modeling, generative models, supervised learning

1. Introduction. Uncertainty quantification (UQ) of parameter estimates in complex systems is critical for comprehensive and interpretable model calibration. In practice, these estimates are frequently derived from incomplete, noisy, or sparse data, either due to inherent limitations in the modeling or constraints in data collection. For complex systems—where underlying behaviors may be highly nonlinear, chaotic, or stochastic—it becomes essential to understand the uncertainty associated with the data-driven parameterizations. Bayesian inference, a powerful probabilistic framework, can be utilized in these potentially ill-posed settings for approximating the conditional distribution of the parameters given the available data.

Traditional methods for parameter estimation such as MCMC [25], require a tractable likelihood and prior density function; the forward physical model is embedded within the likelihood and hence thousands or potentially millions of forward model evaluations may be required in order to achieve convergence to the desired parameter posterior distribution. This method may become intractable when a forward

¹This manuscript has been authored by UT-Battelle, LLC, under contract DE-AC05-00OR22725 with the US Department of Energy (DOE). The US government retains and the publisher, by accepting the article for publication, acknowledges that the US government retains a nonexclusive, paid-up, irrevocable, worldwide license to publish or reproduce the published form of this manuscript, or allow others to do so, for US government purposes. DOE will provide public access to these results of federally sponsored research in accordance with the DOE Public Access Plan. The work of C.Tatsuoka and D.Xiu was partially supported by AFOSR FA9550-22-1-0011.

²Department of Mathematics, The Ohio State University, Columbus, OH 43210, USA (tatsuoka.3@osu.edu, xiu.16@osu.edu).

³Fusion Energy Science Division, Oak Ridge National Laboratory, Oak Ridge, TN, 37831, USA (yangm@ornl.gov).

⁴Computer Science and Mathematics Division, Oak Ridge National Laboratory, Oak Ridge, TN, 37831, USA (zhangg@ornl.gov).

evaluation of the underlying system is computationally expensive, requiring excessive run-times to converge. Alternative approaches such as variational inference [9] similarly require tractable likelihoods and repeated simulations during optimization of the evidence lower bound (ELBO) for obtaining the posterior density approximation. Other likelihood-free methods, such as approximate Bayesian computation (ABC), rely on rejection algorithms based on summary statistics of the forward model, again requiring a large number of forward simulation runs [53].

As a result of these potential limitations, there has been a growing interest in developing machine-learning (ML) based uncertainty quantification methods, which can help mitigate the described efficiency issues while providing robust uncertainty quantification on parameter estimates. One approach is to introduce fast surrogate models, such as trained neural networks, to accelerate forward model evaluations within MCMC [1, 18, 58, 59]. While potentially reducing computational costs, the surrogate model must be globally accurate across the entire parameter domain to ensure reliable posterior samples, and hence sufficient training of such a surrogate model can become a challenge when the available data is sparse, noisy or incomplete. Generative modeling is a form of ML which has seen success in many applications, including image processing [17, 24, 29, 54, 55], anomaly detection [42, 51] and natural language processing [2, 30, 39]. Generative modeling architectures include variational auto-encoders (VAEs), generative adversarial networks (GANs), normalizing flows, and the diffusion model. VAEs enable generative modeling by using encoder-decoder architectures to transform samples to their low-dimensional, latent space representations for learning of the latent probability distribution, which is then used for sampling in parameter space via the decoder [13, 32, 61]. This approach, however, may lead to a loss of interpretability and potential mode collapse due to insufficient information retained in the latent space. Normalizing flows have been extensively applied in uncertainty quantification (UQ) [31, 38, 43, 57, 62], leveraging invertible and differentiable transformations for mapping a standard Gaussian distribution to a desired target distribution. Despite the many advancements in flow designs, the requirement of tractable inverse maps and determinant of the maps' Jacobian matrix may limit the expressivity of these models and also result in high computational costs. GANs have also seen success for posterior sample generation [12, 24, 44], however, the unsupervised training for optimization of the adversarial loss function can lead to mode collapse and may require entropic regularization [6, 33, 50, 63].

Diffusion models learn to generate samples from the target distribution by sequentially injecting noise into the available data samples, and subsequently learning to de-noise the corrupted data in a reverse process. It has seen a wide-range of extensions and has been successful in applications, see [3, 34, 49, 56]. Particularly, score-based diffusion models, presented in [55], has been adapted to UQ for complex systems [4, 36, 37], using an efficient Monte Carlo estimator of the score function, allowing for a training-free diffusion model. While score-based diffusion models traditionally use a neural network to approximate the score function, the lack of labeled data mapping samples from the initial distribution to samples from the terminal distribution within the stochastic process motivates the use of unsupervised learning algorithms, in turn requiring the storage of numerous stochastic paths of the forward SDE and increasing computational costs. Instead, by introducing a Monte Carlo estimator, one can efficiently learn the score-function at each temporal location when solving the reverse-time process. The reverse-time SDE is additionally replaced by the corresponding reverse-time ODE [40], allowing for a deterministic mapping between

initial and terminal states of the samples. This enables the supervised learning of a generative model, taken to be a simple feed forward neural network. After training, the generative model can act as an efficient approximation tool of the target posterior density [37]. This method was further extended in [21, 37] for amortized Bayesian inference [64], allowing for posterior density approximations over a wide-range of observations.

Developments in multi-fidelity modeling for UQ have also been largely motivated by the need for efficient, reliable methods to address the high costs associated with generating large quantities of high-fidelity data for outer-loop applications. In the multi-fidelity setting for parameter estimation, one aims to quantify the uncertainty of the high-fidelity model parameters by leveraging an available low-fidelity model. Multi-fidelity modeling has been studied extensively in the field of UQ [46, 47, 48], where the low-fidelity models are constructed via surrogate models [22, 45], reduced order models, [13, 14, 15], or simplified models such as coarse-grid discretizations [19, 23, 28].

Informative sampling of the parameter space becomes imperative for efficient use of computational resources when attempting to accurately approximate the posterior distribution of the high-fidelity model’s parameter values. Hence, we propose the following multi-fidelity framework: first, a low-fidelity generative model is developed to perform amortized Bayesian inference, offering fast and efficient approximation of target posterior distributions across a wide range of observation values through a single neural network. The low-fidelity generative model’s ability to conduct such rapid posterior density approximations resolves much of the computational burden associated with traditional Bayesian methodologies. The training data set is considered low-fidelity due to the sparsity of data samples and/or the low-resolution numerical solvers used to generate data. If the results of the low-fidelity approximation are sufficient, the user does not need to build the high-fidelity model. However, if a higher-fidelity approximation is required for a specific data observation of interest, the low-fidelity model enables refined sampling of the parameter space, reducing the overall computational overhead by narrowing the sampling domain to regions of high probability of the target posterior density of interest. The high-fidelity solver is used given the refined data set to generate output values and train the high-fidelity, unconditional generative model. The proposed method combines efficient posterior sample generation with adaptive refinement of posterior density approximations, allowing for both speed and accuracy.

The remainder of the paper is organized as follows: in Section 2 we present the problem setting and motivation. In section 3, we review preliminaries, specifically recalling the training-free diffusion model methodologies proposed in [36, 37]. Section 4 presents numerous numerical examples to demonstrate the effectiveness in of the method, and in Section 5 we provide concluding remarks.

2. Problem setting. We setup the parameter estimation problem for a general physical model. Let $x \in \Omega \subset \mathbb{R}^s$ be the spatial variable with the support Ω a bounded domain with a sufficiently smooth boundary, and let $T > 0$ be a finite time horizon. We are interested in estimating the parameter, denoted by $\theta \in \mathbb{R}^d$, of the following differential equation:

$$\mathcal{L}[u(x, t, \theta); \theta] = 0, \quad x \in \Omega, \quad t \in [0, T], \quad (2.1)$$

where \mathcal{L} is a (nonlinear) differential operator and $u(x, t, \theta)$ is the solution of the differential equation belonging to an appropriate Sobolev space, such as $H^1(\Omega)$, ensuring

sufficient regularity. The parameter $\theta \in \Gamma \subset \mathbb{R}^d$ is a d -dimensional vector defined in a compact set $\Gamma \subset \mathbb{R}^d$. We assume that for each $\theta \in \Gamma$, there exists a unique solution $u(x, t, \theta)$ that satisfies the differential equation $\mathcal{L}[u(x, t, \theta); \theta] = 0$, subject to suitable initial and boundary conditions. This uniqueness and well-posedness property is a standard assumption, often guaranteed by classical results in partial differential equations and dynamical systems theory.

In real-world applications, the parameter θ is not directly observable, we need to estimate θ using information obtained via an observation operator, denoted by

$$y = \mathcal{H}(u(x, t, \theta)) + \varepsilon, \quad (2.2)$$

where the mapping $\mathcal{H} : \Omega \times [0, T] \times \Gamma \rightarrow \mathbb{R}^q$ associates the solution u and parameter θ to an observable quantity y , and ε is the observation noise. This operator often represents measurements of the system, such as sensor outputs, integral measurements over subdomains, or pointwise evaluations at specified spatial locations.

The parameter estimation problem is defined in the Bayesian manner. Specifically, we assume that the parameter θ has a prior probability density function, denoted by $p_{\Theta}(\theta)$ supported on Γ , and a likelihood function corresponding to the observation operator in Eq. (2.2), i.e.,

$$p_{Y|\Theta}(y|\theta) \propto \exp \left[-\frac{1}{2} (y - \mathcal{H}(u(x, t, \theta)))^{\top} \Sigma^{-1} (y - \mathcal{H}(u(x, t, \theta))) \right], \quad (2.3)$$

where Θ and Y are the random variables corresponding to the model parameter θ and the observable quantity y , respectively, and Σ is the covariance matrix characterizing the noise statistics in the measurements. Given an observation $Y = y$, the posterior distribution of the parameter θ is obtained through Bayes' theorem:

$$p_{\Theta|Y}(\theta|y) \propto p_{Y|\Theta}(y|\theta) p_{\Theta}(\theta), \quad (2.4)$$

encapsulates both the observational information and the prior assumptions on the unknown parameters. In practice, this posterior distribution often forms the basis for various Bayesian inference techniques, including Markov Chain Monte Carlo sampling, variational inference, and surrogate modeling approaches.

Quantifying the resulting uncertainty in input or parameter information is essential for predictive modeling. However, this uncertainty quantification becomes computationally challenging when the numerical solver for solution u in Eq. (2.1) is expensive. The Bayesian approach to inverse problems provides a rigorous foundation for inference from noisy and incomplete data, with Markov Chain Monte Carlo (MCMC) being particularly valuable for sampling from posterior distributions that often lack closed-form solutions. However, a significant limitation arises: for each new observation y , one must re-run the entire MCMC sampling procedure. To overcome this computational challenge, we propose the development of a multifidelity generative model that enables amortized Bayesian inference through score-based diffusion models. For any observation $y \sim p_Y(y)$, our proposed generative model can directly sample from the posterior distribution $p_{\Theta|Y}$ without requiring repeated simulations. The framework offers both low- and high-fidelity sampling options, with the high-fidelity option requiring only an additional one-time training cost. The detailed architecture and implementation of this multi-fidelity generative model will be discussed in Section 3.

3. Multi-fidelity parameter estimation using conditional diffusion models. In this paper, we propose a novel multi-fidelity framework for parameter estimation that addresses the key computational challenges in Bayesian inference. Our approach involves two generative models, denoted by

$$\theta|y = G^{\text{low}}(y, z) \quad \text{and} \quad \theta = G^{\text{high}}(z), \quad (3.1)$$

where G^{low} is a low-fidelity generative model, G^{high} a high-fidelity generative model, and $z \in \mathbb{R}^d$ a random variable with the standard normal distribution $\mathcal{N}(0, \mathbf{I}_d)$. The low-fidelity generative model $G^{\text{low}}(y, z)$ provides a computationally efficient approach to approximate the posterior distribution $p_{\Theta|Y}(\theta|y)$ across the entire space of possible observations $y \sim p_Y(y)$. Unlike traditional MCMC methods that require new sampling chains for each new observation, the low-fidelity model provides rapid posterior approximations through a single trained network. While $G^{\text{low}}(y, z)$ may not achieve the desired accuracy threshold for certain observations, its ability to identify high-probability regions of $p_{\Theta|Y}(\theta|y)$ can be used as a good proposal distribution, effectively narrowing the search space for more accurate sampling of $p_{\Theta|Y}(\theta|y)$ for a fixed y . The samples generated from these high-probability regions can be used as additional training data for constructing the high-fidelity generative model $G^{\text{high}}(z)$, ensuring that computational resources are focused on the most relevant regions of the parameter space. The proposed workflow is illustrated in Figure 3.1.

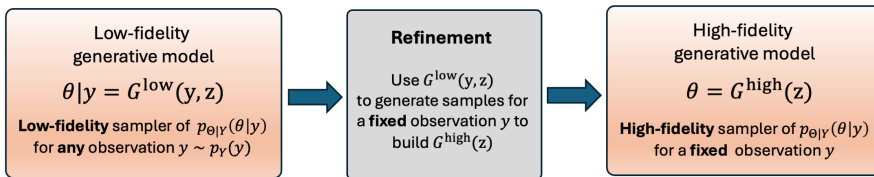


Fig. 3.1: Illustration of the proposed multi-fidelity parameter estimation framework. The low-fidelity generative model efficiently approximates the posterior distribution $p_{\Theta|Y}(\theta|y)$ for any observation $y \sim p_Y(y)$, offering substantial computational advantages over traditional MCMC sampling which requires new runs for each observation. When $G^{\text{low}}(y, z)$ cannot achieve the desired accuracy for a specific observation, it can still guide the sampling process by identifying high-probability regions of $p_{\Theta|Y}(\theta|y)$. These samples then serve as additional training data for constructing the more accurate high-fidelity generative model $G^{\text{high}}(z)$.

The key innovation of the proposed method lies in its adaptive nature. The low-fidelity model serves as an initial rapid approximation tool, capable of handling diverse observation scenarios without the computational overhead typically associated with MCMC methods. This initial approximation is particularly useful in scenarios requiring real-time parameter estimation or when dealing with large-scale inference problems. The high-fidelity model of our method activates selectively, targeting cases where enhanced accuracy is crucial. By utilizing the low-fidelity model’s output to refine the sampling space, we can reduce the computational burden typically associated with the high-fidelity modeling. In this work, we use the training-free score-based diffusion model [36, 35, 5] to build both the low-fidelity and high-fidelity generative models. Section 3.1 provides a brief overview of the score-based diffusion model. Section 3.2 introduces the construction of a low-fidelity generative model using a conditional diffusion model with a training-free score estimator. Section 3.3 describes

how to exploit the low-fidelity generative model as a proposal distribution to build a high-fidelity generative model.

3.1. Overview of the score-based diffusion model. We briefly overview the score-based diffusion model used in this paper and refer to [55] for details. The diffusion model consists of a forward SDE and a reverse SDE defined within a bounded pseudo-temporal domain $\tau \in [0, 1]$. The forward SDE is a Ornstein–Uhlenbeck process, defined by

$$dZ_\tau = b(\tau)Z_\tau d\tau + \sigma(\tau)dW_\tau, \quad \text{with } Z_0 = \Theta|Y \text{ and } Z_1 = Z, \quad (3.2)$$

where the initial condition Z_0 is the target random variable $\Theta|Y$ defined by the posterior distribution in Eq. (2.4). By choosing the appropriate drift and diffusion coefficients $b(\tau)$ and σ_τ as follows:

$$b(\tau) = \frac{d \log \alpha_\tau}{d\tau}, \quad \sigma^2(\tau) = \frac{d\beta_\tau^2}{d\tau} - 2\frac{d \log \alpha_\tau}{d\tau} \beta_\tau^2 \quad \text{with } \alpha_\tau = 1 - \tau, \beta_\tau^2 = \tau, \quad (3.3)$$

the forward SDE can transport the target distribution $Z_0 = \Theta|Y \sim p_{\Theta|Y}(\theta|y)$ to the standard normal distribution $Z_1 = Z \sim \mathcal{N}(0, \mathbf{I}_d)$ [55, 5]. However, what we need is the transport map from Z_1 to Z_0 . To this end, we define the reverse SDE as follows:

$$dZ_\tau = [b(\tau)Z_\tau - \sigma^2(\tau)S(Z_\tau, \tau)] d\tau + \sigma(\tau)dB_\tau \quad \text{with } Z_0 = \Theta|Y \text{ and } Z_1 = Z, \quad (3.4)$$

where B_τ denotes the reverse-time Brownian motion and $S(z_\tau, \tau)$ is the score function defined by,

$$S(z_\tau, \tau) := \nabla_z \log q_{Z_\tau}(z_\tau), \quad (3.5)$$

with $q_{Z_\tau}(z_\tau)$ being the probability density function of the states of the forward SDE (3.2) at any fixed time τ . This reverse SDE acts as a denoiser, allowing for the generation of new samples from the target distribution by transporting samples from the standard normal distribution. The key step is the approximation of the score function; while traditionally approximated by a neural network, this can be a computationally intensive task as it relies on an unsupervised learning algorithm, requiring many iterations of forward SDE paths for learning of the score function. Thus, we utilize the training-free Monte Carlo estimator approach for approximating the score function, as described in the following section.

3.2. Construction of the low-fidelity generative model. This section describes how to use the score-based diffusion model to construct the low-fidelity generative model in Eq. (3.1). The procedure consists of three steps.

Step 1: Collecting samples of the joint distribution $p_{\Theta, Y}(\theta, y)$. In this work, we assume that all samples are generated by solving the underlying differential equation in Eq. (2.1). We first generate a set of samples, denoted by $\{\theta^{(n)}\}_{n=1}^{N_{\text{prior}}}$ from the prior distribution $p_\Theta(\theta)$ in Eq. (2.4). For each $\theta^{(n)}$ we solve the differential equation in Eq. (2.1) and evaluate the observation operator in Eq. (2.2) to obtain the corresponding observation value $y^{(n)}$. The pair $(\theta^{(n)}, y^{(n)})$ is one sample from the joint distribution $p_{\Theta, Y}(\theta, y)$, and the set of prior samples is defined by

$$\mathcal{S}_{\text{prior}} = \left\{ \left(\theta^{(n)}, y^{(n)} \right) \right\}_{n=1}^{N_{\text{prior}}}. \quad (3.6)$$

The prior sample set $\mathcal{S}_{\text{prior}}$ can be viewed as a low-fidelity sample set from two perspectives. First, to reduce the cost of solving the underlying differential equation, we could use a low-fidelity numerical solver (e.g., with low-order spatial/temporal discretization schemes) to generate the observation data $y^{(n)}$, enabling us to afford more prior data for denser coverage of the prior domain Γ . Second, the support of the prior distribution Γ usually covers a large domain in the parameter space due to the lack of prior physical knowledge about the parameter θ , such that the sample set $\{\theta^{(n)}\}_{n=1}^{N_{\text{prior}}}$ may not provide sufficiently dense coverage of the prior domain Γ , especially in high-dimensional settings. The overly large distance between samples in the prior data set usually leads to over-estimation (low-fidelity estimation) of the uncertainty of the posterior distribution.

Step 2: Generating labeled data using the training-free diffusion model.

This step uses the prior data set $\mathcal{S}_{\text{prior}}$ in Eq. (3.6) to generate labeled data for supervised learning of the low-fidelity model $G^{\text{low}}(y, z)$ (3.1), to be used in the next step. The desired labeled data set is denoted by

$$\mathcal{S}_{\text{label}} = \left\{ \left(y^{(m)}, z^{(m)}, \theta^{(m)} \right) : m = 1, \dots, M \right\}, \quad (3.7)$$

where $y^{(m)}$ is a sample from $p_Y(y)$, $z^{(m)}$ is a sample from $\mathcal{N}(0, \mathbf{I}_d)$, and $\theta^{(m)}$ is a sample from the conditional distribution $p_{\Theta|Y}(\theta|y)$. Compared to Eq.(3.1), we can see that $(y^{(m)}, z^{(m)})$ is the input and $\theta^{(m)}$ is the output of the low-fidelity model. Because the low-fidelity model $G^{\text{low}}(y, z)$ is a deterministic function, we need the labeled data set $\mathcal{S}_{\text{label}}$ to represent a relatively smooth functional relationship. However, since the reverse SDE in Eq.(3.4) does not provide the desired smooth functional relationship between the initial and terminal states, we instead use the corresponding reverse ODE to generate the labeled data, i.e.,

$$dZ_\tau = \left[b(\tau)Z_\tau - \frac{1}{2}\sigma^2(\tau)S(Z_\tau, \tau) \right] dt \quad \text{with} \quad Z_0 = \Theta|Y \quad \text{and} \quad Z_1 = Z, \quad (3.8)$$

which provides the same probability flow as the reverse SDE as well as a smooth function relationship between the initial and the terminal states.

To evaluate the score function in Eq. (3.8), we can re-write the probability density function of $q_{Z_\tau}(z_\tau)$ in Eq. (3.5) as an integral, i.e.,

$$q_{Z_\tau}(z_\tau) = \int_{\mathbb{R}^d} q_{Z_\tau, Z_0}(z_\tau, z_0) dz_0 = \int_{\mathbb{R}^d} q_{Z_\tau|Z_0}(z_\tau|z_0) q_{Z_0}(z_0) dz_0, \quad (3.9)$$

where the conditional distribution $q_{Z_\tau|Z_0}(z_\tau|z_0)$ is a Gaussian distribution $Z_\tau|Z_0 \sim \mathcal{N}(\alpha_\tau Z_0, \beta_\tau^2 \mathbf{I}_d)$ and $q_{Z_0}(z_0) = p_{\Theta|Y}(\theta|y)$ is the target distribution. Substituting Eq. (3.9) and Eq. (2.4) into Eq. (3.5), we can re-write the score function as

$$\begin{aligned} S(z_\tau, \tau) &= \nabla_z \log \left(\int_{\mathbb{R}^d} q_{Z_\tau|Z_0}(z_\tau|z_0) q_{Z_0}(z_0) dz_0 \right) \\ &= \frac{1}{\int_{\mathbb{R}^d} q_{Z_\tau|Z_0}(z_\tau|\bar{z}_0) q_{Z_0}(\bar{z}_0) d\bar{z}_0} \int_{\mathbb{R}^d} -\frac{z_\tau - \alpha_\tau z_0}{\beta_\tau^2} q_{Z_\tau|Z_0}(z_\tau|z_0) q_{Z_0}(z_0) dz_0 \\ &= \int_{\mathbb{R}^d} -\frac{z_\tau - \alpha_\tau z_0}{\beta_\tau^2} w(z_\tau, z_0) dz_0, \end{aligned} \quad (3.10)$$

where the weight function $w(z_\tau, z_0)$ is defined by exploiting that $q_{Z_0}(z_0) = p_{\Theta|Y}(\theta|y)$, i.e.,

$$w(z_\tau, z_0) := \frac{q_{Z_\tau|Z_0}(z_\tau|z_0)q_{Z_0}(z_0)}{\int_{\mathbb{R}^d} q_{Z_\tau|Z_0}(z_\tau|\bar{z}_0)q_{Z_0}(\bar{z}_0)d\bar{z}_0} = \frac{q_{Z_\tau|\Theta,Y}(z_\tau|\theta, y) p_{Y|\Theta}(y|\theta) p_\Theta(\theta)}{\int_{\mathbb{R}^d} q_{Z_\tau|\Theta,Y}(z_\tau|\bar{\theta}, y) p_{Y|\Theta}(y|\bar{\theta}) p_\Theta(\bar{\theta})d\bar{\theta}} \quad (3.11)$$

with $\int_{\mathbb{R}^d} w(z_\tau, z_0)q_{Z_0}(z_0)dz_0 = 1$. We can use the prior sample set $\mathcal{S}_{\text{prior}}$ to perform Monte Carlo estimation of the integrals in Eq. (3.10) and Eq. (3.11). Specifically, for any fixed y , the Monte Carlo estimator for the score function is defined by

$$S(z_\tau, \tau) \approx S^{\text{MC}}(z_\tau, \tau) := \sum_{n=1}^{N_{\text{prior}}} -\frac{z_\tau - \alpha_\tau \theta^{(n)}}{\beta_\tau^2} w^{\text{MC}}(z_\tau, \theta^{(n)}|y), \quad (3.12)$$

with the weight function's approximation w^{MC} defined by

$$w^{\text{MC}}(z_\tau, \theta^{(n)}|y) := \frac{\exp\left\{-\frac{(z_\tau - \alpha_\tau \theta^{(n)})^2}{2\beta_\tau^2}\right\} \exp\left(-(y - y^{(n)})^\top \Sigma^{-1}(y - y^{(n)})\right)}{\sum_{n'=1}^{N_{\text{prior}}} \exp\left\{-\frac{(z_\tau - \alpha_\tau \theta^{(n')})^2}{2\beta_\tau^2}\right\} \exp\left(-(y - y^{(n')})^\top \Sigma^{-1}(y - y^{(n')})\right)}, \quad (3.13)$$

where Σ is the covariance matrix of the observation noise defined in the likelihood function in Eq. (2.3), and $(x^{(n)}, y^{(n)})$ are from the prior data set $\mathcal{S}_{\text{prior}}$ in Eq. (3.6).

With the score estimator in Eq. (3.12), the procedure for generating the labeled data set $\mathcal{S}_{\text{label}}$ can be summarized as follows. For $m = 1, \dots, M$, we first generate one sample $y^{(m)}$ from $p_Y(y)$, which can be done by running another unconditional training-free diffusion model using the marginal sample set $\{y^{(n)}\}_{n=1}^{N_{\text{prior}}}$ in Eq. (3.6). Then, we generate one sample $z^{(m)}$ from $\mathcal{N}(0, \mathbf{I}_d)$. Next, we set $Z_1 = z^{(m)}$ and $Y = y^{(m)}$ in Eq. (3.8) and solve the reverse ODE and define z_0 as the labeled data $\theta^{(m)}$ in Eq. (3.7).

Step 3: Supervised learning of the low-fidelity model using the labeled data. Once $\mathcal{S}_{\text{label}}$ is built, we train a fully-connected neural network model using the standard mean squared error loss to obtain the desired low-fidelity generative model $G^{\text{low}}(y, z)$. This conditional generative model is capable of providing efficient posterior samples from the target distribution $p_{\Theta|Y}(\theta|y)$ for any given data observation of interest $Y = y$ from the distribution $p_Y(y)$. In practice, if the low-fidelity model provides satisfactory results for a specific parameter estimation problem, the user of this method does not need to use the high-fidelity model. Otherwise, they will use the low-fidelity model as a good starting point to build the high-fidelity model.

3.3. Construction of the high-fidelity generative model. Because the prior data set $\mathcal{S}_{\text{prior}}$ may not provide sufficiently dense coverage of the prior domain Γ or the prior data may be generated by a potentially low-fidelity model, the low-fidelity generative model G^{low} may overestimate uncertainty when approximating the target conditional distribution $p_{\Theta|Y}(\theta|y)$ for a fix observation of interest $Y = y$. Hence, if a higher-fidelity approximation to the specific target conditional density $p_{\Theta|Y}(\theta|y)$ is desired, the following refinement procedure can be conducted to obtain the high-fidelity generative model $G^{\text{high}}(z)$. The key idea is to use the distribution defined by $G^{\text{low}}(y, z)$ for the fixed observation y as the prior distribution and refine the score estimation in Eq. (3.12) and Eq. (3.13). The procedure consists of the following steps.

- Use the low-fidelity generative model $G^{\text{low}}(y, z)$ constructed in Section 3.2 to generate a set of refined prior samples, denoted by $\{\theta^{(k)}\}_{k=1}^K$, for the fixed y .
- Perform kernel density estimation based on the samples $\{\theta^{(k)}\}_{k=1}^K$ to obtain an approximation to the probability density function, denoted by $p_{\Theta}^{\text{KDE}}(\theta)$ determined by $G^{\text{low}}(y, z)$.
- Based on samples $\{\theta^{(k)}\}_{k=1}^K$ (where K is typically taken to be quite high for the KDE approximation and can be generated cheaply using G^{low}), take a refined data set of size $N_{\text{refine}} < K$ and solve the differential equation in Eq. (2.1) with a high-fidelity solver to obtain the corresponding observation values $\{y^{(n)}\}_{n=1}^{N_{\text{refine}}}$. Note that $y^{(n)}$ will be close to the fixed observation y but not exactly equal to it due to the inaccuracy of the low-fidelity model.
- Generate a refined labeled data set, denoted by

$$\mathcal{S}_{\text{refine}} = \left\{ \left(z^{(n)}, \theta^{(n)} \right) : n = 1, \dots, N_{\text{refine}} \right\}, \quad (3.14)$$

by solving the reverse ODE for the fixed y and using the updated estimators for the score function, i.e.,

$$S^{\text{high}}(z_{\tau}, \tau) := \sum_{n=1}^{N_{\text{refine}}} -\frac{z_{\tau} - \alpha_{\tau}\theta^{(n)}}{\beta_{\tau}^2} w^{\text{high}}(z_{\tau}, \theta^{(n)}|y), \quad (3.15)$$

with the weight function’s approximation w^{high} defined by

$$w^{\text{high}}(z_{\tau}, \theta^{(n)}|y) := \frac{\exp\left\{-\frac{(z_{\tau} - \alpha_{\tau}\theta^{(n)})^2}{2\beta_{\tau}^2}\right\} \exp\left(-\frac{(y - y^{(n)})^{\top} \Sigma^{-1} (y - y^{(n)})}{2\beta_{\tau}^2}\right) \frac{p_{\Theta}(\theta^{(n)})}{p_{\Theta}^{\text{KDE}}(\theta^{(n)})}}{\sum_{n'=1}^{N_{\text{refine}}} \exp\left\{-\frac{(z_{\tau} - \alpha_{\tau}\theta^{(n')})^2}{2\beta_{\tau}^2}\right\} \exp\left(-\frac{(y - y^{(n')})^{\top} \Sigma^{-1} (y - y^{(n')})}{2\beta_{\tau}^2}\right) \frac{p_{\Theta}(\theta^{(n')})}{p_{\Theta}^{\text{KDE}}(\theta^{(n')})}}, \quad (3.16)$$

where $p_{\Theta}(\theta)$ is the prior probability density function and $p_{\Theta}^{\text{KDE}}(\theta)$ is the kernel density estimation of the sample set $\{\theta^{(k)}\}_{k=1}^K$.

- Use the new labeled data $\mathcal{S}_{\text{refine}}$ to train another fully-connected neural network to obtain the high-fidelity generative model $G^{\text{high}}(z)$.

Once trained, the high-fidelity generative model $G^{\text{high}}(z)$ is capable of efficiently mapping samples from the standard Gaussian distribution to the target distribution $p_{\Theta|Y}(\theta|y)$ for a fixed y with improved accuracy over the low-fidelity model $G^{\text{low}}(y, z)$. However, the improved accuracy is only valid for a specific observation y . The above procedure needs to be repeated if we need to obtain the high-fidelity model for another observation value.

4. Numerical Experiments. In this section, we present numerical experiments to demonstrate the effectiveness of the proposed method. The results of the proposed multi-fidelity approach are compared against ground-truth data when available, or against those by Markov chain Monte Carlo (MCMC) method obtained via Python `emcee` package <https://emcee.readthedocs.io/en/stable>. To account for uncertainties encountered in real-world, we add white noise to the observed data when the system lacks explicit randomness. The example in Section 4.1 benchmarks the accuracy of our method for a problem with known analytical ground-truth solution. Wall-clock times are computed by running our code on a server equipped with NVIDIA Tesla V100-PCIE with a GPU card of 32GB of memory. Unless otherwise noted, the generative neural network models are taken to be a single layer, fully connected feed-forward neural network with 20 neurons and are trained for 10,000 epochs using the Adam optimizer with learning rate of 10^{-3} .

4.1. 1D Illustrative Example. In this subsection, we verify the accuracy of the proposed algorithm using an illustrative example with known analytical solution. The dynamical system and observation operator are defined as follows:

$$\mathcal{L}[u(\theta)] = u(\theta) - \theta^2 = 0, \quad \mathcal{H}(u(\theta)) = \theta^2, \quad \theta \in \Gamma = [-10, 10]. \quad (4.1)$$

The noisy observation y is expressed as:

$$y = \hat{\mathcal{H}}(u(\theta)) = \mathcal{H}(u(\theta)) + \epsilon = \theta^2 + \epsilon, \quad (4.2)$$

where the noise ϵ follows a Gaussian distribution, $\mathcal{N}(0, \sigma^2)$, with $\sigma^2 = 0.1$. The objective is to approximate the conditional distribution $p_{\Theta|Y}(\theta|y)$ for a given observation y . The exact conditional distribution is:

$$p_{\Theta|Y}(\theta|y) = \frac{p_{Y|\Theta}(y|\theta)p_{\Theta}(\theta)}{p_Y(y)} = \frac{e^{-\frac{(y-\theta^2)^2}{2\sigma^2}} \mathbf{1}_{[-10,10]}(\theta)}{\int_{-\infty}^{\infty} e^{-\frac{(y-\theta^2)^2}{2\sigma^2}} d\theta}. \quad (4.3)$$

This analytical solution allows us to assess the accuracy of the proposed method.

The dynamical system \mathcal{L} has an explicit form that can be solved directly. Therefore, the main difference between low- and high-resolution simulations lies in the spatial discretization of samples from Γ . For training the low-fidelity diffusion model $G^{\text{low}}(y, z)$, we construct a training data set $\mathcal{S}_{\text{prior}} = \{\theta^{(n)}, y^{(n)}\}_{n=1}^{N_{\text{prior}}}$, where $y^{(n)}$ is defined by Eq. (4.2). Specifically, we sample uniformly spaced points $\theta^{(n)}$ with a resolution of $\Delta\theta = 0.2$ across the domain $\Gamma = [-10, 10]$, yielding $N_{\text{prior}} = 101$ samples. Using this data set, we simulate the reverse ODE in Eq. (3.8) to obtain labeled data for training the low-fidelity generative model $G^{\text{low}}(y, z)$. Once trained, G^{low} can generate the low-fidelity density function for any observation $y \sim p_Y(y)$.

To train the high-fidelity generative model $G^{\text{high}}(z)$ for a specific observation y , we first use G^{low} to generate the refined prior samples $\{\theta^{(k)}\}_{k=1}^K$, where $K = 10000$. These samples are used to obtain the probability density function approximation $p_{\Theta}^{\text{KDE}}(\theta)$ in Figs. 4.1 and 4.2. Based on this data set, we form $\mathcal{S}_{\text{refine}} = \{\theta^{(n)}, y^{(n)}\}_{n=1}^{N_{\text{refine}}}$, with $y^{(n)} = \hat{\mathcal{H}}(u(\theta^{(n)}))$ and $N_{\text{refine}} = 1000$. Specifically, these data samples are taken to be uniformly spaced points over the range of refined prior samples $\{\theta^{(k)}\}_{k=1}^K$. The refined data set $\mathcal{S}_{\text{refine}}$ adapts dynamically to the specific observation y .

Using the trained multi-fidelity models G^{low} and G^{high} , we test the approximation for different observations y . Figs. 4.1 and 4.2 show the conditional distributions $p_{\Theta|Y}(\theta|y)$ for $y = 1$ and $y = 9$ respectively. The left panels depict samples generated by the low-fidelity model G^{low} , the middle columns are samples generated by solving the reverse-ODE using $\mathcal{S}_{\text{refine}}$ in the score function approximation, and the right panels are samples generated from the high-fidelity generative model G^{high} for a specific data observation y . Despite limited training data, the low-fidelity model G^{low} provides reasonable approximations, effectively capturing the parameter domain for the observation of interest. The high-fidelity model G^{high} , benefiting from higher-resolution samples, achieves accurate approximations of the true distribution, with KL divergence controlled to be on the order of 10^{-3} and 10^{-2} for $y = 1$ and $y = 9$ respectively. The KL divergence, used to quantify the difference between the exact distribution p_{exact} and the approximate distribution p_{approx} , is defined as:

$$D_{\text{KL}}(p_{\text{exact}}|p_{\text{approx}}) = \int_{-\infty}^{\infty} p_{\text{exact}}(x) \log \left(\frac{p_{\text{exact}}(x)}{p_{\text{approx}}(x)} \right) dx. \quad (4.4)$$

This integral is approximated using a Riemann sum over a uniform mesh. In Table 4.1, we record the wall-clock times for different stages of the method to demonstrate its efficiency for sample generation. It demonstrates that the multi-fidelity diffusion model efficiently generates parameter samples for the observations of interest.

| Model | Data labeling | Training $G^{(\cdot)}$ | Synthesizing 10K samples |
|-------------------------|---------------|------------------------|--------------------------|
| G^{low} | 0.25 seconds | 8.17 seconds | 4.40e-04 seconds |
| $G^{\text{high}} y = 1$ | 6.73 seconds | 8.37 seconds | 4.42e-04 seconds |
| $G^{\text{high}} y = 9$ | 6.76 seconds | 8.39 seconds | 3.96e-04 seconds |

Table 4.1: Wall-clock run-time for different computational stages of the proposed diffusion model. Data labeling refers to running the reverse-time ODE for training data. Training $G^{(\cdot)}$ refers to the training time of the neural network model. Synthesizing 10K samples refers to the run-time for neural network $G^{(\cdot)}$ to generate 10K samples. For G^{low} , this is the average run time to synthesize the 10K samples for the two observations of interest. The run-times demonstrates that the multi-fidelity diffusion model efficiently generates parameter samples for the observations of interest.

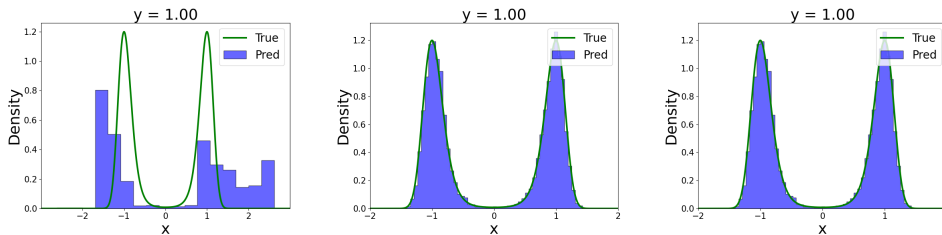


Fig. 4.1: The condition distribution $p_{\Theta|Y}(\theta|y)$ for $y = 1$. Left panel shows the density approximation obtained via the low-fidelity generative model G^{low} . The KL divergence, computed according to Eq. (4.4) using a uniform mesh (1000 samples over $[-2, 2]$), is 2.118. The middle panel displays the density approximation derived from labeled data by solving the reverse-time ODE model, yielding a KL divergence of 2.32e-03. The right panel presents the density approximation generated by the high-fidelity generative model G^{high} , which achieves a KL divergence of 2.23e-03. The small KL divergence values for both the ODE solution and G^{high} indicate excellent approximation performance, with G^{high} demonstrating particularly strong fidelity to the true density.

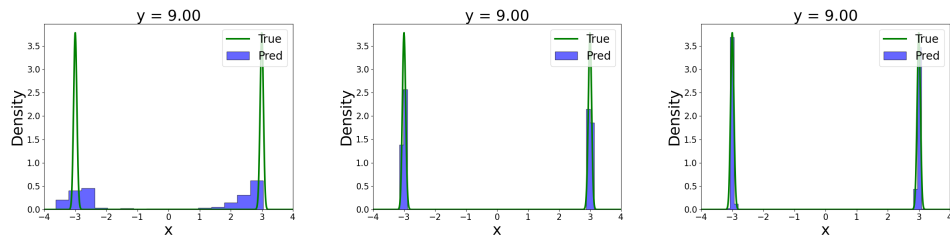


Fig. 4.2: The condition distribution $p_{\Theta|Y}(\theta|y)$ for $y = 9$. Left panel shows the density approximation obtained via the low-fidelity generative model G^{low} . The KL divergence, computed according to Eq. (4.4) using a uniform mesh (1000 samples over $[-4, 4]$), is 3.341. The middle panel displays the density approximation derived from labeled data by solving the reverse-time ODE model, yielding a KL divergence of $1.22\text{e-}02$. The right panel presents the density approximation generated by the high-fidelity generative model G^{high} , which achieves a KL divergence of $2.78\text{e-}02$. The small KL divergence values for both the ODE solution and G^{high} indicate excellent approximation performance, with G^{high} demonstrating particularly strong fidelity to the true density.

4.2. Viscous Burgers. The solution to the viscous Burgers partial differential equation at equilibrium with perturbed boundary conditions is investigated, where θ represents the unknown viscosity parameter. The governing equations and observation operator are formulated as:

$$\begin{cases} \mathcal{L}[u(x, t, \theta); \theta] = u_t(x, t, \theta) + u_x(x, t, \theta) - \theta u_{xx}(x, t, \theta) = 0, \\ \mathcal{H}(u(x, t, \theta)) = [u(x_1, T, \theta), \dots, u(x_L, T, \theta)]^\top, \\ x \in \Omega = [-1, 1], \quad t \in [0, T], \quad \theta \in \Gamma = [0.01, 0.1], \end{cases} \quad (4.5)$$

where Ω denotes the spatial domain, Γ represents the admissible range of the viscosity parameter θ , and L denotes the number of sensor locations within spatial domain Ω . The Dirichlet boundary conditions are prescribed as:

$$u(-1, t) = 1 + \delta, \quad u(1, t) = -1, \quad t \in [0, T], \quad (4.6)$$

where $\delta = 0.01$ represents the boundary perturbation magnitude. The observation operator maps the solution to discrete observations at L sensor locations at time T . The noise-contaminated observations \mathbf{y} are expressed as:

$$\mathbf{y} = \hat{\mathcal{H}}(u(x, t, \theta)) = \mathcal{H}(u(x, t, \theta)) + \epsilon = [u(x_1, T, \theta) + \epsilon_1, \dots, u(x_L, T, \theta) + \epsilon_L]^\top. \quad (4.7)$$

The measurement noise $\epsilon = [\epsilon_1, \dots, \epsilon_L]^\top$ is characterized by a multivariate Gaussian distribution $\mathcal{N}(\mathbf{0}, \Sigma)$, with covariance matrix $\Sigma = \mathbf{I} \cdot \sigma^2 \in \mathbb{R}^{L \times L}$ and standard deviation $\sigma = 0.01$. Specifically, measurements are collected at $L = 21$ uniformly distributed sensor locations across the subdomain $\hat{\Omega} = [0, 1]$ with spatial resolution $\Delta x = 0.05$. The objective is to approximate the posterior distribution $p_{\Theta|Y}(\theta|\mathbf{y})$.

For the specified perturbation $\delta = 0.01$, a reference distribution is constructed to evaluate the accuracy of the proposed method. The solution of Eq. (4.5) at equilibrium

for fixed θ is given by:

$$u(x, \theta) = -A \tanh \left[\frac{A}{2\theta} (x - z_{\text{ex}}) \right], \quad (4.8)$$

where z_{ex} denotes the location of the transition layer where $u(z_{\text{ex}}, \theta) = 0$ and $-A = \frac{\partial u}{\partial x}|_{x=z_{\text{ex}}}$ is the slope at this location. This setting follows the super-sensitivity UQ problem studied in [60].

To construct a reference distribution conditioned on data observation of interest \mathbf{y} , we utilize MCMC by defining the following negative log-likelihood and assuming a uniform prior $p(\theta)$:

$$-\log \mathcal{L}(\theta) = \frac{1}{2} [(\mathbf{y} - \mathcal{H}(u(x, t, \theta)))^\top \Sigma^{-1} (\mathbf{y} - \mathcal{H}(u(x, t, \theta)))], \quad (4.9)$$

where \mathcal{H} is determined by Eq.(4.8) at the L sensor locations. We obtain 10,000 samples from the posterior to perform KDE estimation.

For numerical implementation, the Burgers equation is discretized using finite differences on a uniform grid comprising of N_{grid} points, where N_{grid} varies between low- and high-fidelity models. The temporal discretization is semi-implicit Euler method with time step $\Delta t = 0.01$. The simulation terminates after 5×10^4 time steps (upon reaching $T = 500$). The low-fidelity diffusion model training data set $\mathcal{S}_{\text{prior}} = \{\theta^{(n)}, \mathbf{y}^{(n)}\}_{n=1}^{N_{\text{prior}}}$ is constructed where $\mathbf{y}^{(n)}$ follows Eq. (4.7). The parameter values $\theta^{(n)}$ are sampled uniformly with resolution $\Delta\theta = 9 \times 10^{-4}$ across $\Gamma = [0.01, 0.1]$, yielding $N_{\text{prior}} = 101$ samples. The corresponding $\mathbf{y}^{(n)}$ values at time T are obtained by first solving Eq. (4.5) using a spatial discretization of $N_{\text{grid}} = 400$ points. Noisy measurement data are then collected at the $L = 21$ sensor locations. The low-fidelity model G^{low} generates refined prior samples $\{\theta^{(k)}\}_{k=1}^K$ with $K = 10000$ to generate the probability density approximation.

For the high-fidelity diffusion model, given an observation \mathbf{y} , we build $\mathcal{S}_{\text{refine}} = \{\theta^{(n)}, \mathbf{y}^{(n)}\}_{n=1}^{N_{\text{refine}}}$ where $N_{\text{refine}} = 200$ samples are uniformly distributed across the range of $\{\theta^{(k)}\}_{k=1}^K$ samples. The $\mathbf{y}^{(n)}$ values are computed at time T by solving Eq. (4.5) using a finer spatial discretization of $N_{\text{grid}} = 800$ points and then collecting data at the noisy sensor locations.

The performance of both low- and high-fidelity generative models is evaluated using data $\mathbf{y}_{|\theta=0.05}$ and $\mathbf{y}_{|\theta=0.07}$, obtained by solving Eq. (4.5) using $N_{\text{grid}} = 800$ with viscosity values $\theta = 0.05$ and $\theta = 0.07$ respectively. Results presented in Fig. 4.3 demonstrate that the low-fidelity model provides an adequate initial approximation of the target density and identifies the relevant parameter domain. For both test cases, the Kullback-Leibler divergence between the reference and high-fidelity approximation distributions is of order 10^{-2} , indicating accurate approximation by the high-fidelity model. Table. 4.2 presents the computational cost for each stage of the method, demonstrating efficient sampling from the posterior distribution $p_{\Theta|Y}(\theta|\mathbf{y})$ when compared to the runtime of MCMC. The results demonstrate the efficiency of our method in reducing computational costs while preserving accuracy in sampling from the posterior density.

4.3. Lorenz 63 System. Consider the three-dimensional Lorenz 63 system, which is known for exhibiting chaotic behavior. The system dynamics and observation

| Model | Data labeling | Training $G^{(\cdot)}$ | Synthesizing 10K samples |
|---|---------------|------------------------|--------------------------|
| G^{low} | 0.23 seconds | 1.59 seconds | 7.30e-04 seconds |
| $G^{\text{high}} \mathbf{y} _{\theta=0.05}$ | 0.40 seconds | 7.90 seconds | 3.49e-04 seconds |
| MCMC | N/A | N/A | 9.92 seconds |
| $G^{\text{high}} \mathbf{y} _{\theta=0.07}$ | 0.56 seconds | 9.19 seconds | 6.23e-04 seconds |
| MCMC | N/A | N/A | 10.31 seconds |

Table 4.2: Wall-clock run-time for different computational stages of the viscous Burgers example. Data labeling refers to running the reverse-time ODE for training data. Training $G^{(\cdot)}$ refers to the training time of the neural network model (G^{low} is trained for approximately 1300 epochs using early stopping with a validation split of 20% and patience of 1000 epochs, while G^{high} models are trained for 10000 epochs). Synthesizing 10K samples refers to the run-time for neural network $G^{(\cdot)}$ to generate 10K samples. For G^{low} , this is the average run time to synthesize the 10K samples for the two observations of interest. The results demonstrate the computational efficiency of the multi-level sampling approach for the viscous Burgers equation.

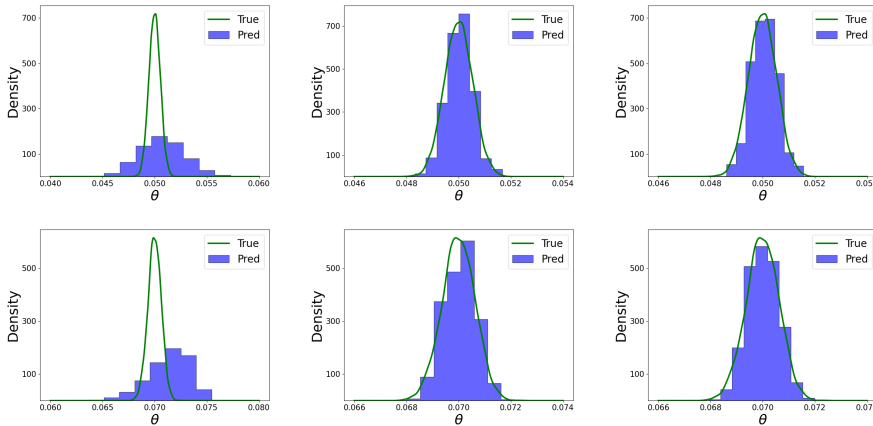


Fig. 4.3: The conditional distribution $p_{\Theta|Y}(\theta|\mathbf{y})$ for $\mathbf{y}|_{\theta=0.05}$ and $\mathbf{y}|_{\theta=0.07}$. For observation $\mathbf{y}|_{\theta=0.05}$ (top row): The left panel shows the density approximation obtained via the low-fidelity generative model G^{low} . The KL divergence, computed using a uniform mesh (1000 samples over $[0.04, 0.06]$), is 0.96. The middle panel displays the density approximation derived from labeled data generated by solving the reverse-time ODE model, yielding a KL divergence of 3.11×10^{-2} . The right panel presents the density approximation generated by the high-fidelity model G^{high} , which achieves a KL divergence of 3.07×10^{-2} . For observation $\mathbf{y}|_{\nu=0.07}$ (bottom row): The left panel shows the density approximation from G^{low} with a KL divergence of 1.11 (1000 samples over $[0.06, 0.08]$). The middle panel shows the ODE-based approximation with a KL divergence of 1.38×10^{-2} , and the right panel presents the G^{high} approximation with a KL divergence of 1.39×10^{-2} . The results demonstrate that both the ODE-based solution and G^{high} provide significantly more accurate approximations as evidenced by their substantially lower KL divergence values.

operator are given by:

$$\begin{cases} \mathcal{L}[u(t, \theta); \theta] = \begin{bmatrix} \dot{u}_1 - h(\gamma)(u_2 - u_1) \\ \dot{u}_2 - (u_1(\rho - u_3) - y_2) \\ \dot{u}_3 - (u_1 u_2 - \beta u_3) \end{bmatrix} = \begin{bmatrix} 0 \\ 0 \\ 0 \end{bmatrix}, & u(t_0) = u_0, \\ \mathcal{H}(u(t, \theta)) = u_1(t, \theta), \\ t \in [0, T], \quad \theta = (\gamma, \rho) \in \Gamma = [-5, 5] \times [20, 30] \end{cases} \quad (4.10)$$

where $\theta = (\gamma, \rho)$ represents the unknown parameters, and we fix $\beta = 2$. The observation operator \mathcal{H} simulates the scenario in which only partial observation of the underlying system is feasible, i.e. for $u = [u_1, u_2, u_3]^\top \in \mathbb{R}^3$, we only observe solution trajectories of u_1 . The function $h(\gamma) = \gamma^2$ relates to the parameter γ , and \dot{u} denotes the time derivative. The initial condition is set to $u_0 = [-10, 5, 20]^\top$, and the time domain is defined as $T = 1$. The observations \mathbf{y} consist of $(L + 1)$ noisy measurements of the u_1 solution trajectory over time:

$$\mathbf{y} = \hat{\mathcal{H}}(u(t, \theta)) = \mathcal{H}(u(t, \theta)) + \epsilon = [u_1(t_0; \theta) + \epsilon_0, \dots, u_1(t_L; \theta) + \epsilon_L]. \quad (4.11)$$

The measurements are taken at uniform time intervals of $\Delta t = 0.02$, resulting in $(L+1) = 51$ observations over the time domain. The additive noise $\epsilon = [\epsilon_0, \epsilon_1, \dots, \epsilon_L]^\top$ is a vector of mean zero Gaussian random variables with covariance $\Sigma \in \mathbb{R}^{(L+1) \times (L+1)}$, $\Sigma = \mathbf{I} \cdot \sigma^2$ for $\mathbf{I} \in \mathbb{R}^{(L+1) \times (L+1)}$ with $\sigma^2 = 0.1$. The goal is to approximate the two-dimensional target distribution $p_{\Theta|Y}(\theta|\mathbf{y})$ for parameters $\theta = (\gamma, \rho)$ given the data observation \mathbf{y} .

For the multi-fidelity diffusion model training, we employ different spatial resolutions for the parameter space $\theta = (\gamma, \rho)$. For the low-fidelity generative model $G^{\text{low}}(y, z)$, we construct the training data set $\mathcal{S}_{\text{prior}} = \{\theta^{(n)}, \mathbf{y}^{(n)}\}_{n=1}^{N_{\text{prior}}}$ by sampling the 81×81 uniform grid over the parameter domain $\Gamma = [-5, 5] \times [20, 30]$ with spatial resolution $\Delta\gamma = \Delta\rho = 0.25$, yielding $N_{\text{prior}} = 6561$ samples. Using this data set and the reverse ODE simulation, we obtain the labeled training data for G^{low} . The trained G^{low} is then used to generate the refined prior data set $\{\theta^{(k)}\}_{k=1}^K$ with $K = 10000$ for density approximation.

For the high-fidelity model training, we refine the spatial resolution over the parameter domain to $\Delta\gamma = \Delta\rho = 0.05$, a five-fold increase in resolution compared to the low-fidelity model. The refined training data set $\mathcal{S}_{\text{refine}} = \{\theta^{(n)}, \mathbf{y}^{(n)}\}_{n=1}^{N_{\text{refine}}}$ is constructed by selecting parameters uniformly distributed across the range of the refined domain. This approach ensures that the high-fidelity model is trained with more precise parameter sampling in the region of interest, leading to improved accuracy in the final density approximations.

We evaluate the low- and high-fidelity generative models using two different observations \mathbf{y}_1 and \mathbf{y}_2 , obtained by solving Eq. (4.10) with parameters $(\gamma, \rho) = (\sqrt{7}, 25)$ and $(\gamma, \rho) = (\sqrt{10}, 28)$, respectively. The high-fidelity model training uses refined data sets with $N_{\text{refine}} = 5762$ and $N_{\text{refine}} = 8817$ samples for the two cases respectively. The expected bimodal behavior centered at $(\pm\gamma, \rho)$ in this system arises from its symmetry properties. This symmetry, combined with the chaotic nature of the system, naturally leads to two equally probable parameter regions that can produce similar observations, resulting in an evenly distributed bimodal posterior distribution. In Figs. 4.4 and 4.5, it is observed that while MCMC sampling (using a burn-in of

20,000 and 10 walkers) struggles to capture this symmetric bimodal structure, the score-based diffusion model more effectively reveals this fundamental characteristic of the system. The comparative wall-clock run-times for these methods are recorded in Table 4.3.

| Model | Data labeling | Training $G^{(\cdot)}$ | Synthesizing 10K samples |
|--------------------------------|---------------|------------------------|--------------------------|
| G^{low} | 1.75 seconds | 7.99 seconds | 8.08e-04 seconds |
| $G^{\text{high}} \mathbf{y}_1$ | 32.92 seconds | 8.16 seconds | 4.27e-04 seconds |
| MCMC | N/A | N/A | 105.10 seconds |
| $G^{\text{high}} \mathbf{y}_2$ | 53.16 seconds | 8.23 seconds | 4.29e-04 seconds |
| MCMC | N/A | N/A | 113.35 seconds |

Table 4.3: Wall-clock run-time for different computational stages of the chaotic ODE (Lorenz 63) example. Data labeling refers to running the reverse-time ODE for training data Training $G^{(\cdot)}$ refers to the training time of the neural network model. For data labeling, we used $N_{\text{refine}} = 5762$ samples for observation \mathbf{y}_1 and $N_{\text{refine}} = 8817$ samples for observation \mathbf{y}_2 in the score function approximation. Synthesizing 10K samples refers to the run-time for neural network $G^{(\cdot)}$ (MCMC) to generate 10K samples. For G^{low} , this is the average run time to synthesize the 10K samples for the two observations of interest. The results demonstrate the computational efficiency of generating parameter samples for the chaotic ODE system.

4.4. Linear SDE. In this section, we consider the one dimensional Ornstein–Uhlenbeck process defined as,

$$\begin{cases} \mathcal{L}[Y_t(\theta); \theta] = dY_t - (h(\mu) - Y_t)dt - g(\sigma)dW_t = 0, & Y_0 = y, \\ t \in [0, T], & \theta = (\mu, \sigma) \in \Gamma = [-10, 10] \times [-10, 10] \end{cases} \quad (4.12)$$

where $T = 1$ and $\theta = (\mu, \sigma)$ are unknown parameters of interest. We define h as a function of unknown parameter μ and g as a function of unknown parameter σ . Specifically we fix $h(\mu) = \mu^2$ and $g(\sigma) = \sigma^2$ and the initial condition as $Y_0 = 1.5$. The observation operator \mathcal{H} is defined by the statistics of solution Y at time T , i.e.,

$$\mathbf{y} = \mathcal{H}(Y_t(\theta)) = [\mathbb{E}[Y_T|\theta], S[Y_T|\theta]]^\top \quad (4.13)$$

where $\mathbb{E}[\cdot|\theta]$ denotes the conditional expectation given parameter θ and $S[\cdot|\theta]$ refers to the conditional standard deviation.

To numerically quantify the observation \mathbf{y} , we consider the Monte-Carlo approximation of \mathcal{H} . Using the Euler–Maruyama method with N_{MC} simulation paths, we estimate the statistics in Eq. (4.13) for fixed θ , where N_{MC} is an adjustable hyper-parameter controlling the accuracy of the simulation. The Monte Carlo approximation is given by:

$$\mathcal{H}^{\text{MC}}(Y_t(\theta)) = \left[\tilde{\mathbb{E}}[Y_T|\theta], \tilde{S}[Y_T|\theta] \right]^\top = \left[\frac{\sum_{i=1}^{N_{\text{MC}}} Y_T^{(i)}(\theta)}{N_{\text{MC}}}, \sqrt{\frac{\sum_{i=1}^{N_{\text{MC}}} (Y_T^{(i)}(\theta) - \tilde{\mathbb{E}}[Y_T|\theta])^2}{N_{\text{MC}} - 1}} \right]^\top, \quad (4.14)$$

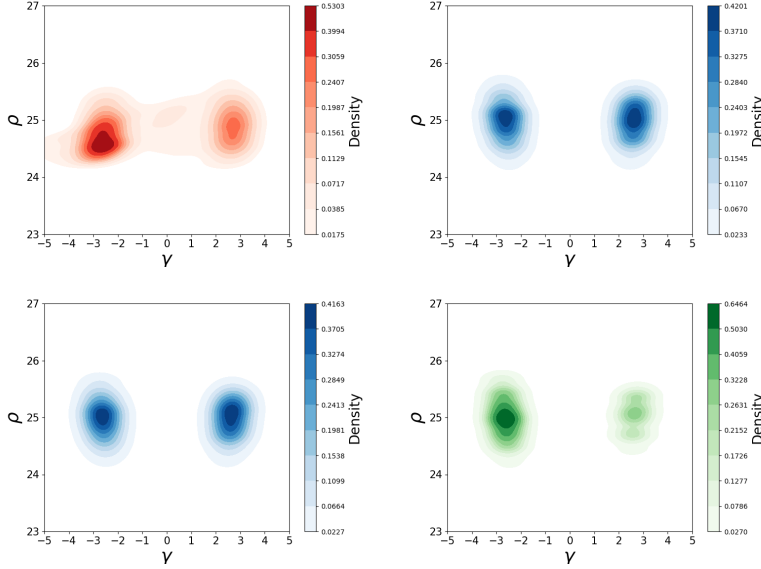


Fig. 4.4: Density approximations for observation \mathbf{y}_1 , generated using parameters $(\gamma, \rho) = (\sqrt{7}, 25)$. The bimodal structure centers at $(-\sqrt{7}, 25)$ and $(\sqrt{7}, 25)$, reflecting the symmetry of the Lorenz system where both (γ, ρ) and $(-\gamma, \rho)$ produce equivalent dynamics. Top left: Density approximation obtained via the low-fidelity generative model $G^{\text{low}}(y, z)$, trained using 81×81 parameter pairs over domain $D = [-5, 5] \times [20, 30]$ (6561 total samples), showing clear identification of the bimodal structure. Top right: Density approximation using the labeled data set, demonstrating refined accuracy of the bimodal distribution. Bottom left: High-fidelity density approximation generated by $G^{\text{high}}(z)$, exhibiting balanced and well-separated modes, capturing the system’s inherent symmetry. Bottom right: MCMC results using 10 walkers within the refined domain with 20,000 burn-in steps, showing less balanced representation of the bimodal structure compared to our proposed method.

where $Y_T^{(i)}(\theta)$ denotes the position of the i -th trajectory at time T for fixed θ . The output data from the simulation model can then be expressed as:

$$\mathbf{y} = \mathcal{H}^{\text{MC}}(Y_t(\theta)) = \mathcal{H}(Y_t(\theta)) + \epsilon, \quad (4.15)$$

where $\epsilon \sim \mathcal{N}(0, \Sigma)$ represents the Monte Carlo estimation error. To understand the uncertainty in our parameter estimates due to this model error, we approximate the covariance matrix Σ as:

$$\Sigma \approx \hat{\Sigma} = \begin{bmatrix} \frac{1}{N_{\text{grid}}} \sum_{i=1}^{N_{\text{grid}}} (\bar{\mathbb{E}}[Y_T|\theta] - \mathbb{E}[Y_T|\theta])^2 & 0 \\ 0 & \frac{1}{N_{\text{grid}}} \sum_{i=1}^{N_{\text{grid}}} (\bar{S}[Y_T|\theta] - S[Y_T|\theta])^2 \end{bmatrix}, \quad (4.16)$$

where $N_{\text{grid}} = 20$ points are randomly sampled from the parameter domain Γ . Since we assume no access to the exact form of the SDE in (4.12), we use $N_{\text{MC}} = 10^5$ simulations to obtain the ground truth statistics in Eq. (4.16).

The goal is to approximate the posterior density $p_{\Theta|Y}(\theta|\mathbf{y})$ for a given observation \mathbf{y} . While the expectation $\mathbb{E}[\cdot]$ and standard deviation $S[\cdot]$ of the solution Y_T of

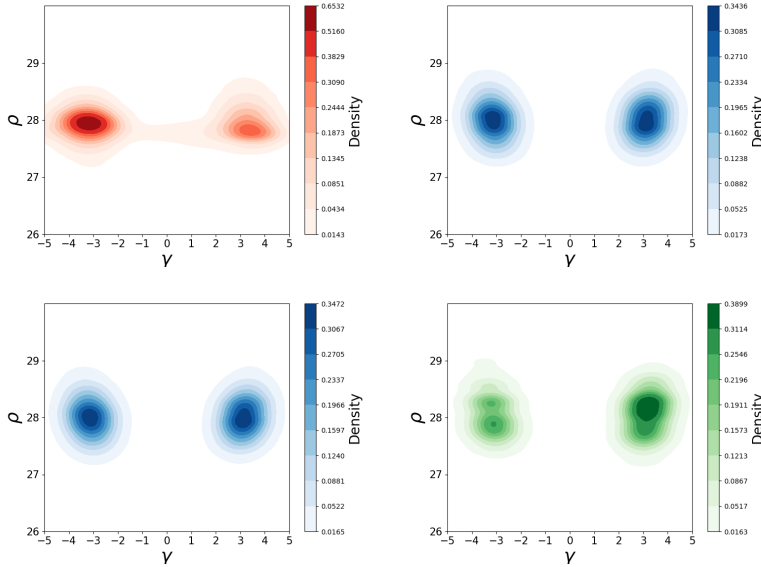


Fig. 4.5: Density approximations for observation \mathbf{y}_2 , generated using parameters $(\gamma, \rho) = (\sqrt{10}, 28)$. The bimodal structure centers at $(-\sqrt{10}, 28)$ and $(\sqrt{10}, 28)$, reflecting the symmetry of the Lorenz system where both (γ, ρ) and $(-\gamma, \rho)$ produce equivalent dynamics. Top left: Density approximation obtained via generative model $G^{\text{low}}(y, z)$, trained using 81×81 parameter pairs $\theta = (\gamma, \rho)$ over domain $D = [-5, 5] \times [20, 30]$ (6561 total samples). Top right: Density approximation using labeled data set. Bottom left: Density approximation generated by $G^{\text{high}}(z)$. Bottom right: MCMC results using 10 walkers within refined domain with 20,000 burn-in steps.

Eq. (4.12) can be computed exactly for known θ , our data-driven setting assumes the governing SDE is unknown. Thus, we rely solely on numerical simulation to generate input-output pairs for parameter estimation.

The generation of training data for both low- and high-fidelity models differs from two aspects. The resolution of the parameter domain Γ and the accuracy of the Euler–Maruyama method controlled by N_{MC} . For the low-fidelity generative model G^{low} , we construct the training data set $\mathcal{S}_{\text{prior}} = \{\theta^{(n)}, \mathbf{y}^{(n)}\}_{n=1}^{N_{\text{prior}}}$ by sampling a uniform 41×41 grid over $\Theta = [-10, 10] \times [-10, 10]$ with mesh size $\Delta\mu = \Delta\sigma = 0.5$, yielding $N_{\text{prior}} = 1681$ samples. We then generate corresponding outputs $\mathbf{y}^{(n)}$ using the Euler–Maruyama method with $N_{\text{MC}} = 2000$ paths in Eq. (4.14). For a given observation \mathbf{y} , again we construct the kernel density estimate from samples generated by G^{low} . From this data set, we construct the refined data set $\mathcal{S}_{\text{refine}} = \{\theta^{(n)}, \mathbf{y}^{(n)}\}_{n=1}^{N_{\text{refine}}}$ by refining the spatial resolution in parameter domain to $\Delta\mu = \Delta\sigma = 0.1$ and sampling over the refined domain, given by the range of the G^{low} outputs. The high-fidelity outputs $\mathbf{y}^{(n)}$ are generated using $N_{\text{MC}} = 10000$ paths in Eq. (4.14).

The quadratic nature of functions h and g implies that the target density should exhibit four equal modes centered at $(\pm\mu, \pm\sigma)$. We demonstrate our method’s performance using two test cases with observations $\mathbf{y}_1 = [3.081 \ 0.658]^\top$ and $\mathbf{y}_2 =$

$[1.462 \ 0.059]^\top$, corresponding to true parameters $\theta = [2 \ 1]^\top$ and $\theta = [1.2 \ 0.3]^\top$, respectively. Figs. 4.6 and 4.7 demonstrate the accuracy of our approach compared to MCMC sampling. For the MCMC comparison, we employ a surrogate model in the likelihood computation, specifically a single-layer fully connected neural network with 100 neurons. This surrogate is trained on 201×201 samples from the parameter domain Γ , using $\Delta\mu = \Delta\sigma = 0.1$ spatial resolution and the high-fidelity simulation with $N_{\text{MC}} = 10,000$. The MCMC implementation uses 10 walkers restricted to the identified refined region for each example. The figures clearly show that our score-based method successfully captures the expected four-fold symmetry of the modes, while MCMC struggles to identify this symmetric structure in the posterior distribution. The computational efficiency of our approach is summarized in Table 4.4, which presents wall-clock times for both methods. The results demonstrate that our method achieves significant computational savings for posterior sampling, while maintaining accuracy in sampling from the target posterior distribution.

| Model | Data labeling | Training $G^{(\cdot)}$ | Synthesizing 10K samples |
|--------------------------------|---------------|------------------------|--------------------------|
| G^{low} | 8.31 seconds | 8.23 seconds | 1.07e-03 seconds |
| $G^{\text{high}} \mathbf{y}_1$ | 16.97 seconds | 8.11 seconds | 4.20e-04 seconds |
| MCMC | N/A | N/A | 20.20 seconds |
| $G^{\text{high}} \mathbf{y}_2$ | 17.79 seconds | 8.04 seconds | 4.09e-04 seconds |
| MCMC | N/A | N/A | 23.48 seconds |

Table 4.4: Wall-clock run-times for different computational stages of the Ornstein-Uhlenbeck example. Data labeling refers to running the reverse-time ODE for training data. For data labeling, we used $N_{\text{refine}} = 3320$ samples for observation \mathbf{y}_1 and $N_{\text{refine}} = 3250$ samples for observation \mathbf{y}_2 in the score function approximation. Training $G^{(\cdot)}$ refers to the training time of the neural network model (all network models are trained for 10000 epochs). Synthesizing 10K samples refers to the run-time for neural network $G^{(\cdot)}$ (MCMC) to generate 10K samples. For G^{low} , this is the average run time to synthesize the 10K samples for the two observations of interest. The results demonstrate the computational efficiency of our method in generating parameter samples for the stochastic differential equation system.

4.5. Runaway electron (RE) dissipation with impurity injection. Runaway electrons (REs) pose a significant threat to the safety and integrity of fusion reactors due to their high energies, which can cause severe damage to the reactor’s walls and components [16]. One effective method to mitigate the dangers posed by REs is the use of impurity injection, e.g., shattered pellet injection (SPI) [52]. SPI introduces high-Z impurities into the plasma, rapidly increasing the electron density and encouraging RE dissipation through collisions. The Fokker-Planck (FP) differential with collision operators describes the evolution of electron distribution function $f(p, \eta, r, t)$ in momentum magnitude p , pitch angle η , and minor radius r ,

$$\mathcal{L}[f(p, \eta, r, t, \theta); \theta] = \frac{\partial f}{\partial t} - \mathcal{C}(f) + \mathcal{E}(f) + \mathcal{R}(f) + \mathcal{S}_{\text{Aval.}}(f) = 0, \quad (4.17)$$

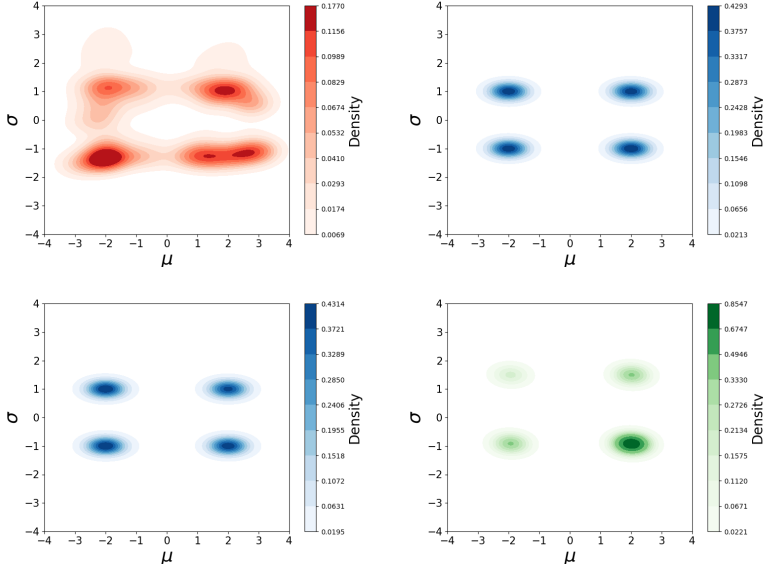


Fig. 4.6: Parameter estimation results for observation \mathbf{y}_1 corresponding to true parameters $(\mu, \sigma) = (2, 1)$. The four panels demonstrate the superior accuracy of our approach compared to MCMC sampling: Top right: Initial low-fidelity generative model $G^{\text{low}}(y, z)$. Top left: Density approximation using labeled data set. Bottom left: Density approximation defined by high-fidelity model $G^{\text{high}}(z)$. Bottom right: MCMC sampling using 10 walkers with 20,000 burn-in steps. Our method successfully captures the expected four equal modes centered at $(\pm\mu, \pm\sigma)$, while MCMC struggles to identify this symmetric structure in the posterior distribution.

where $\mathcal{C}(f)$ is Coulomb (small-angle) collision operator, $\mathcal{E}(f)$ is the electric field acceleration, $\mathcal{R}(f)$ is synchrotron radiation damping, and $\mathcal{S}_{\text{Aval.}}(f)$ is the large-angle collision operator for secondary RE generation.

The Coulomb collisions are a crucial mechanism for runaway electron (RE) dissipation. These collisions, between REs and injected impurities, play a key role in dissipating the energy of REs by increasing their interaction rates with the surrounding plasma. The Coulomb collision operator is defined as

$$\mathcal{C}(f) = \frac{1}{p^2} \frac{\partial}{\partial p} \left[p^2 \left(C_A \frac{\partial f}{\partial p} + C_F f \right) \right] + \frac{C_B}{p^2} \left[\frac{1}{\sin \eta} \frac{\partial}{\partial \eta} \left(\sin \eta \frac{\partial f}{\partial \eta} \right) \right],$$

where C_F , C_A and C_B are linearized transport coefficients for collisional friction, parallel diffusion, and pitch angle scattering, separately. We integrate collision operators by generalizing the coefficients of these operators to include both non-relativistic and relativistic energy limits. With the model of bound electrons and partially ionized

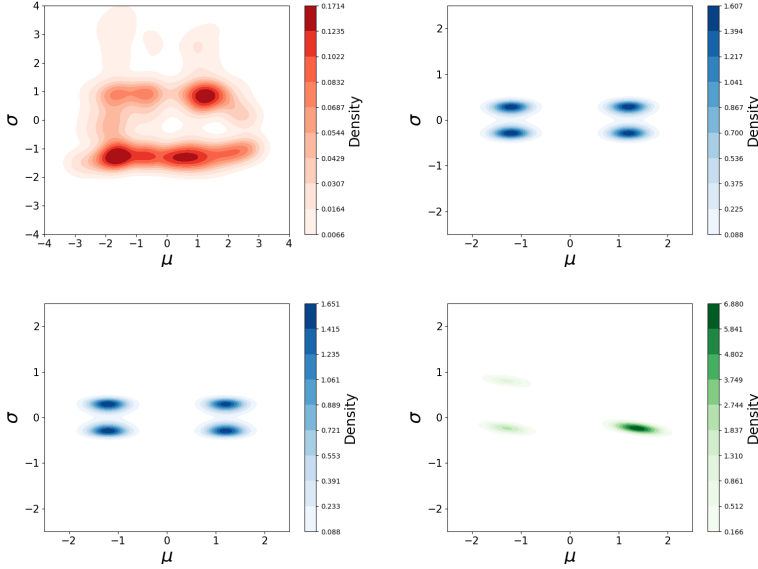


Fig. 4.7: Parameter estimation results for observation \mathbf{y}_2 corresponding to true parameters $(\mu, \sigma) = (1.2, 0.3)$. The four panels demonstrate the superior accuracy of our approach compared to MCMC sampling: Top right: Initial low-fidelity generative model $G^{\text{low}}(y, z)$. Top left: Density approximation using labeled data set. Bottom left: Density approximation defined by high-fidelity model $G^{\text{high}}(z)$. Bottom right: MCMC sampling using 10 walkers with 20,000 burn-in steps. Our method effectively captures the expected four equal modes centered at $(\pm\mu, \pm\sigma)$, while MCMC fails to fully resolve this symmetric structure in the posterior distribution.

impurities [26], the transport coefficients are

$$\begin{aligned}
C_{A,\text{Bound}}(\nu) &= \frac{\Gamma_{ee}\mathcal{G}\left(\frac{\nu}{\nu_{\text{th}}}\right)}{\nu} \\
C_{F,\text{Bound}}(\nu) &= \frac{\Gamma_{ee}\mathcal{G}\left(\frac{\nu}{\nu_{\text{th}}}\right)}{T_e} \left\{ 1 + \sum_j \frac{n_j}{n_e} \frac{Z_j - Z_{0j}}{\ln \Lambda_{ee}} \left[\frac{1}{5} \ln(1 + h_j^5) - \beta^2 \right] \right\} \\
C_{B,\text{Bound}}(\nu) &= \frac{\Gamma_{ei}}{2\nu} Z_{\text{eff}} \left(1 + \frac{1}{Z_{\text{eff}}} \sum_j \frac{n_j}{n_e} \frac{g_j}{\ln \Lambda_{ei}} \right) \\
&\quad + \frac{\Gamma_{ee}}{2\nu} \left[\text{erf}\left(\frac{\nu}{\nu_{\text{th}}}\right) - \mathcal{G}\left(\frac{\nu}{\nu_{\text{th}}}\right) + \frac{1}{2} \left(\frac{\nu_{\text{th}}\nu}{c^2}\right) \right],
\end{aligned}$$

where $\Gamma_{ee,ei} = n_e e^4 \ln \Lambda_{ee,ei} / 4\pi\epsilon_0^2$ with $\ln \Lambda_{ee,ei}$ is the Coulomb logarithm for e-e (e-i) collisions, $\nu_{\text{th}} = \sqrt{2T_e/m_e}$ is the thermal electron velocity, and \mathcal{G} is the Chandrasekhar function. n_j is the density of the j -th ionization state, Z_j is the unscreened (i.e., fully ionized) impurity ion charge, and $Z_{0,j}$ is the screened (i.e., partially ionized) impurity ion charge. $h_j = p\sqrt{\gamma - 1}/(m_e c I_j)$, where I_j is the mean excitation energy and $\beta = \nu/c$ is the relativistic speed. The term $Z_j - Z_{0j}$ is used to define the number of bound electrons a partially ionized impurity charge state possesses. Further details

on this model can be found in Refs. [27, 7, 10, 20, 41] and references therein.

The numerical simulation of the Fokker-Planck equation in Eq. (4.17) is performed using the Kinetic Orbit Runaway electrons Code (KORC) collision operator Monte-Carlo (MC) solver [11]. We adopt a magnetic geometry with a major radius of $R_0 = 2.616$ (m), an on-axis toroidal magnetic field of $B_0 = 3.388$ (T), and a background electron temperature of $T_e = 2$ (eV). To simplify the numerical simulation, we assume the impurity density for the α -species is time-independent and spatially homogeneous. We focus on two impurity species: argon (Ar) and deuterium (D), considering both their neutral forms Ar and D and their partially ionized charge states Ar^{+1} and D^{+1} . For the neutral impurities, we assume constant fixed values of $n_{\text{Ar}} = n_{\text{D}} = 1 \times 10^{19} (\text{m}^{-3})$, while treating $n_{\text{Ar}^{+1}}$ and $n_{\text{D}^{+1}}$ as input variables for the study. Additionally, we assume a spatially and temporally homogeneous electric field E serving as another input variable. In this case, equal impurity densities are applied to both Ar^+ and D^+ ions, with $n_{\text{Ar}^+} = n_{\text{D}^+} = n_{\text{imp}}$. Cases with different impurity densities will be investigated in future work. Consequently, two input parameters $\{\theta^{(i)}\}_{i=1}^N = \{n_{\text{imp}}^{(i)}, E^{(i)}\}_{i=1}^N$ are varied for the study. For a given simulation input parameter set $\theta^{(i)}$, we evolve RE populations $\{(p^{(n)}, \xi^{(n)}, r^{(n)})\}_{n=1}^{N_{\text{MC}}}$ by running KORC Monte-Carlo solver. The initial RE condition corresponds to a 5 MeV monoenergetic, 10° monopitch and the runaway electron density is spatially constant in the normalized radius r . We step the simulation time as $T = 20$ ms. The avalanche term $\mathcal{S}_{\text{Aval.}}(f)$ significantly increases the computational cost of sampling-based numerical methods due to the exponential growth of secondary REs. Therefore, it is essential to explore the multi-fidelity diffusion model to efficiently capture the detailed dynamics in the region of interest.

To characterize the RE ensemble evolution at a macroscopic level, we define the total RE current I_{RE} as [8]

$$I_{\text{RE}} = -\frac{e}{2\pi} \sum_n^{N_{\text{MC}}} \frac{\nu_\phi}{R_n} \mathcal{M}_{\text{RE},n}, \quad \text{where } \mathcal{M}_{\text{RE},n} = \begin{cases} 1, & \text{if } p_n > m_e c \\ 0, & \text{if } p_n < m_e c, \text{ or hits the wall,} \end{cases} \quad (4.18)$$

where $\nu_\phi \simeq \nu \cos \eta$ with pitch angle η . The output of interest is the normalized RE current damping rate $\varphi_{I_{\text{RE}}} = \frac{dI_{\text{RE}}}{dt} \approx \frac{I_{\text{RE}}(T) - I_{\text{RE}}^0}{T}$, which is numerically calculated by linear fitting¹. Overall, for location $X = (p, \eta, r)$, the observational operator is $y = \mathcal{H}(X(\theta))$, where the output is the damping rate $y = \varphi_{I_{\text{RE}}}$, and input parameters are $\theta = (n_{\text{imp}}, E)$. Let N_{MC} denote the number of trajectories of Monte Carlo solver where N_{MC} is an adjustable hyper-parameter of the simulation model. It follows that the Monte Carlo approximation of the observational operator can be written as

$$y = \mathcal{H}^{\text{MC}}(X(\theta)) = \mathcal{H}(X(\theta)) + \epsilon, \quad (4.19)$$

for $\epsilon \sim \mathcal{N}(\mathbf{0}, \Sigma)$ for some covariance matrix Σ . We assume $\mathcal{H}^{\text{MC}}(X(\theta))$ is an asymptotically unbiased estimator of $\mathcal{H}(X(\theta))$ i.e. $\mathbb{E}[\mathcal{H}^{\text{MC}}(X(\theta))] = \mathcal{H}(X(\theta))$ as $N_{\text{MC}} \rightarrow \infty$. Our goal is to compute the conditional distribution $p((n_{\text{imp}}, E) | \varphi_{I_{\text{RE}}})$ given a target damping rate $\varphi_{I_{\text{RE}}}$.

For training the low-fidelity model G^{low} , we first generate data samples using $N_{\text{MC}} = 500$ simulation paths to obtain low-fidelity outputs. We take our ini-

¹In our work, we normalize the RE current I_{RE} by its initial value I_{RE}^0 , i.e., $\bar{I}_{\text{RE}} = I_{\text{RE}}/I_{\text{RE}}^0$. For the simplicity of notation, we omit the overbar for the normalized quantities.

tial sampling domain for (n_{imp}, E) to be a 15×9 uniform grid over the domain $\Gamma = [1e19, 1e20] \times [0.1, 0.9]$ depicted in Fig. 4.8. Hence our low-fidelity prior data set for score function approximation is $\mathcal{S}_{\text{prior}} = \{(\theta^{(i)}, y^{(i)})\}_{i=1}^{N_{\text{prior}}}$ with $N_{\text{prior}} = 135$. It illustrates the effects of the impurity density n_{imp} (x -axis) and electric field magnitude E (y -axis) on the RE current decay rate φ_{RE} . As the electric field amplitude increases, more runaway electrons are generated due to stronger acceleration, resulting in a higher RE current. Conversely, as the impurity density increases, collisions between runaway electrons and impurity ions become more frequent, leading to enhanced energy dissipation and a reduction in RE current. To compute the likelihood in the score function approximation, we require an estimate of Σ in Eq. (4.19), which we approximate using Eq. (4.16) with $N_{\text{grid}} = 20$. Since we do not have access to the ground truth damping rate, we approximate reference values using $N_{\text{MC}} = 60000$. We take the architecture of all generative models in this example to be a single layer, fully-connected feed forward neural network with 100 neurons.

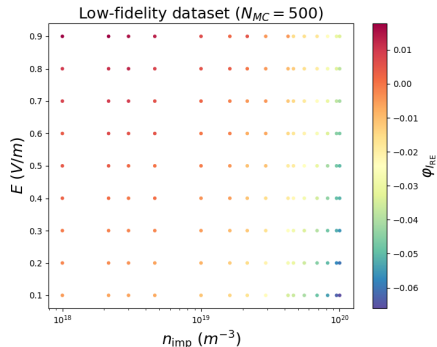


Fig. 4.8: φ_{RE} with varying n_{imp} and E over parameter domain Γ . The training data set is consist of 135 simulation (generated 15×9 grid) shots, with a logarithmic scale in n_{imp} and a linear scale in E . Each simulation shot is performed using $N_{\text{MC}} = 500$ electron trajectories.

Fig. 4.9 illustrates the distribution $p((n_{\text{imp}}, E) | \varphi_{\text{RE}})$ for the target RE current damping rate with specific values of $\varphi_{\text{RE}}^* = 0.01, 0, -0.025$ (from left to right). We compare these results with MCMC predictions using kernel density estimation as a surrogate model constructed from the low-fidelity data set. While good agreement is observed between the MCMC results and the generative model, achieving higher accuracy in specific regions requires further refinement using the high-fidelity solver.

We then employ the high-fidelity solver to examine the target domain in greater detail. The high-fidelity model conducts additional simulations within this domain, using $N_{\text{MC}} = 5000$ electron trajectories per simulation to construct $\mathcal{S}_{\text{refine}}$. The number of samples in $\mathcal{S}_{\text{refine}}$ is determined by the number of fine resolution grid points (using a 64×32 grid) that fall within the range of samples generated by G^{low} for a given data observation y . Figure 4.10 shows the results for $\varphi_{\text{RE}}^* = 0.01, 0, -0.025$. The top row illustrates the distribution of simulation shots in the target domain, while the middle row presents the corresponding contour plots generated from the labeled data set. The bottom row displays the results from the high-fidelity generative model G^{high} . Comparing these results with MCMC predictions using kernel density estimation as a surrogate model constructed from the specified data sets reveals strong

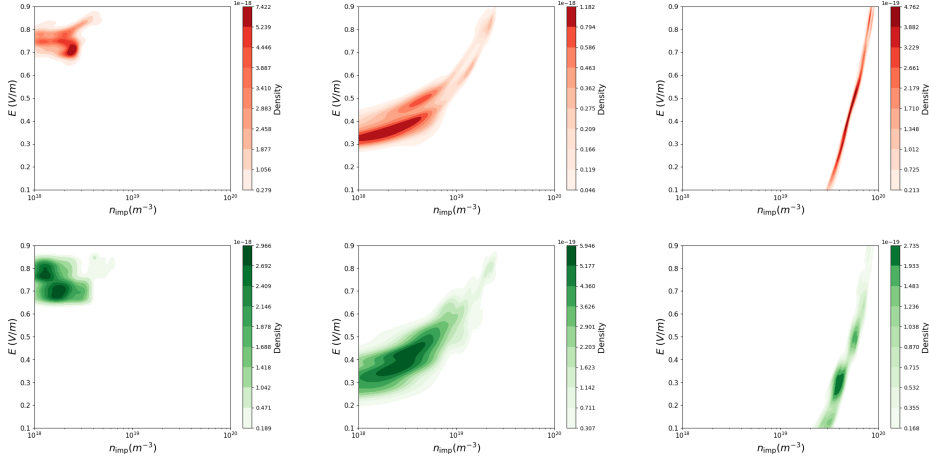


Fig. 4.9: Results from the low-fidelity generative model G^{low} . Top row: Contour plots showing the distribution $p((n_{\text{imp}}, E) | \varphi_{\text{IRE}})$ for target RE current damping rates $\varphi_{\text{IRE}}^* = 0.01, 0, -0.025$ (from left to right). These distributions are generated using the low-fidelity model, which employs both a reduced training data set for the diffusion model and fewer Monte-Carlo trajectories ($N_{\text{MC}} = 500$ electrons per case). Bottom row: Corresponding results from the MCMC algorithm using a surrogate model. While good agreement is observed between the MCMC and generative model results, our method demonstrates significantly faster sample generation. Further refinement using the high-fidelity solver is required to capture additional details within these regions

agreement, indicating that the high-fidelity, score-based diffusion model successfully captures the target distribution. Table 4.5 presents the computational run-times for each stage of our method. The results demonstrate significant computational efficiency in generating posterior samples compared to MCMC, which requires rerunning the entire algorithm for each new sample generation. While good agreement is observed between the MCMC and generative model results, our method demonstrates significantly faster sample generation.

5. Conclusion. We introduced a multi-fidelity method for obtaining posterior distributions of parameter estimates conditioned on data observations of interest. This method leverages low- and high-fidelity models in conjunction with a training-free score-based diffusion model to efficiently generate the posterior density approximation. Supervised learning of neural networks is used to develop low- and high-fidelity generative models capable of efficiently producing samples from the posterior distribution. The conditional low-fidelity generative model enables amortized Bayesian inference for efficient density approximations over a wide range of data observations. The high-fidelity generative model activates selectively when higher accuracy density approximations are required for a specific data observation, utilizing the outputs from the low-fidelity generative model to efficiently sample from the parameter space for building of the high-fidelity training data set. Once trained, the high-fidelity generative model is capable of accurately approximating the target posterior distribution. The effectiveness of the proposed method is demonstrated through several examples of complex systems, including parameter estimation for a plasma physics application

| Model | Data labeling | Training $G^{(\cdot)}$ | Synthesizing 10K samples |
|-------------------------------|---------------|------------------------|--------------------------|
| G^{low} | 1.76 seconds | 8.12 seconds | 4.30e-04 seconds |
| MCMC, $y = 0.01$ | N/A | N/A | 10.02 seconds |
| MCMC, $y = 0$ | N/A | N/A | 9.57 seconds |
| MCMC, $y = -0.025$ | N/A | N/A | 9.80 seconds |
| $G^{\text{high}}, y = 0.01$ | 1.73 seconds | 8.36 seconds | 3.99e-04 seconds |
| MCMC | N/A | N/A | 10.98 seconds |
| $G^{\text{high}}, y = 0$ | 2.61 seconds | 8.13 seconds | 4.33e-04 seconds |
| MCMC | N/A | N/A | 12.15 seconds |
| $G^{\text{high}}, y = -0.025$ | 3.04 seconds | 8.28 seconds | 4.26e-04 seconds |
| MCMC | N/A | N/A | 12.79 seconds |

Table 4.5: Wall-clock run-times for different computational stages of the runaway electron example. Data labeling refers to running the reverse-time ODE for training data. For data labeling, we used the following N_{refine} samples in the score function approximation: $N_{\text{refine}} = 197$ for $y = 0.01$, $N_{\text{refine}} = 461$ for $y = 0$, and $N_{\text{refine}} = 553$ for $y = -0.025$. Training $G^{(\cdot)}$ refers to the training time of the neural network model (all network models are trained for 10000 epochs). Synthesizing 10K samples refers to the run-time for neural network $G^{(\cdot)}$ (MCMC) to generate 10K samples. For G^{low} , this is the average run time to synthesize the 10K samples for the three observations of interest. The results demonstrate the computational efficiency of our method in generating parameter samples for the runaway electron system.

aimed at mitigating runaway electrons, critical for ensuring the safety of fusion reactors. When analytical reference distributions are unavailable, we compare results and wall-clock run-times with the state-of-the-art and widely implemented MCMC algorithm, `emcee`, to highlight the accuracy and efficiency of our method. This flexible framework also provides a foundation for extensions to multi-fidelity applications in parameter estimation, inverse problems, and forward state estimation problems for higher-dimensional physical systems, which will be explored in future studies.

Acknowledgment. This work is supported by the U.S. Department of Energy, Office of Science, Office of Advanced Scientific Computing Research, Applied Mathematics program, under the contract ERKJ443, and accomplished at Oak Ridge National Laboratory (ORNL), and under Grant DE-SC0022254. This material is also partially supported by the U.S. Department of Energy, Office of Science, Office of Workforce Development for Teachers and Scientists, Office of Science Graduate Student Research (SCGSR) program. The SCGSR program is administered by the Oak Ridge Institute for Science and Education for the DOE under contract number DE-SC0014664. ORNL is operated by UT-Battelle, LLC., for the U.S. Department of Energy under Contract DE-AC05-00OR22725.

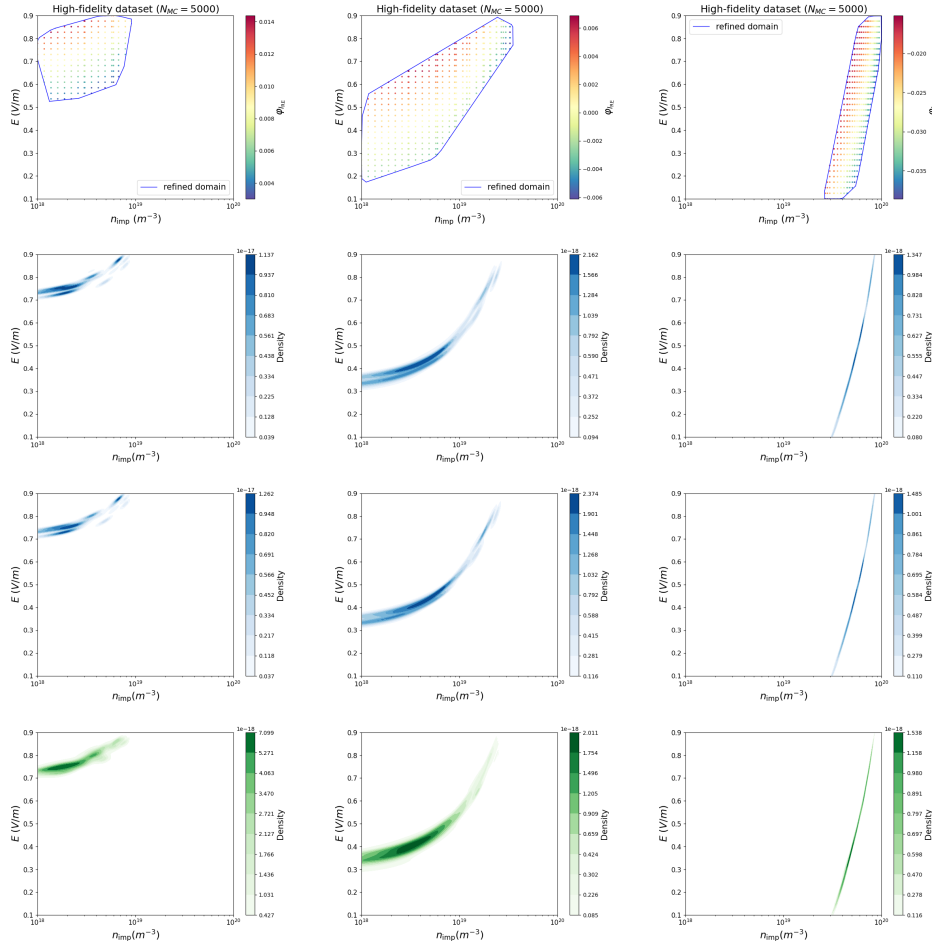


Fig. 4.10: The high-fidelity solver explores the target domain for $\varphi_{IRE}^* = 0.01, 0, -0.025$ using more simulation shots with $N_{MC} = 5000$ electron trajectories per case. Top row: The data samples in $\mathcal{S}_{\text{refine}}$ generated from the range of G^{low} samples. Second row: The contour plot shows the distribution $p((n_{\text{imp}}, E)|\varphi_{IRE}^*)$ for target RE current damping rate with $\varphi_{IRE}^* = 0.01, 0, -0.025$ (from left to right), generated from the labeled data sets. The second iteration results in a refined density approximation of the target distribution. Third row: The contour plots generated by G^{high} , allowing for efficient data sampling from the target distribution. Bottom row: The corresponding results from the MCMC algorithm using a surrogate model and 10 walkers within the refined domain (restricted to range of samples generated by G^{low}). We see good agreement between the results of the diffusion model and MCMC.

REFERENCES

- [1] M. J. ASHER, B. F. CROKE, A. J. JAKEMAN, AND L. J. PEETERS, *A review of surrogate models and their application to groundwater modeling*, Water Resources Research, 51 (2015), pp. 5957–5973.
- [2] J. AUSTIN, D. D. JOHNSON, J. HO, D. TARLOW, AND R. VAN DEN BERG, *Structured denoising diffusion models in discrete state-spaces*, Advances in Neural Information Processing

- Systems, 34 (2021), pp. 17981–17993.
- [3] L. BALDASSARI, A. SIAHKOOHI, J. GARNIER, K. SOLNA, AND M. V. DE HOOP, *Taming score-based diffusion priors for infinite-dimensional nonlinear inverse problems*, arXiv preprint arXiv:2405.15676, (2024).
 - [4] F. BAO, Z. ZHANG, AND G. ZHANG, *A score-based nonlinear filter for data assimilation*, <https://arxiv.org/pdf/2306.09282> (2023), <https://arxiv.org/abs/2306.09282>.
 - [5] F. BAO, Z. ZHANG, AND G. ZHANG, *An ensemble score filter for tracking high-dimensional nonlinear dynamical systems*, Computer Methods in Applied Mechanics and Engineering, 432 (2024), p. 117447.
 - [6] R. BAPTISTA, B. HOSSEINI, N. B. KOVACHKI, AND Y. M. MARZOUK, *Conditional sampling with monotone gans: from generative models to likelihood-free inference*, SIAM/ASA Journal on Uncertainty Quantification, 12 (2024), pp. 868–900.
 - [7] M. BEIDLER, D. DEL CASTILLO-NEGRETE, D. SHIRAKI, L. R. BAYLOR, E. M. HOLLMANN, AND C. LASNIER, *Wall heating by subcritical energetic electrons generated by the runaway electron avalanche source*, Nuclear Fusion, 64 (2024), p. 076038.
 - [8] M. T. BEIDLER, D. DEL-CASTILLO-NEGRETE, L. R. BAYLOR, D. SHIRAKI, AND D. A. SPONG, *Spatially dependent modeling and simulation of runaway electron mitigation in diii-d*, Physics of Plasmas, 27 (2020).
 - [9] D. M. BLEI, A. KUCUKELBIR, AND J. D. MCAULIFFE, *Variational inference: A review for statisticians*, Journal of the American statistical Association, 112 (2017), pp. 859–877.
 - [10] A. H. BOOZER, *Theory of runaway electrons in iter: Equations, important parameters, and implications for mitigation*, Physics of Plasmas, 22 (2015).
 - [11] L. CARBAJAL, D. DEL CASTILLO-NEGRETE, D. SPONG, S. SEAL, AND L. BAYLOR, *Space dependent, full orbit effects on runaway electron dynamics in tokamak plasmas*, Physics of Plasmas, 24 (2017), p. 042512.
 - [12] Y. CHEN AND D. XIU, *Learning stochastic dynamical system via flow map operator*, Journal of Computational Physics, 508 (2024), p. 112984.
 - [13] N. CHENG, O. A. MALIK, S. DE, S. BECKER, AND A. DOOSTAN, *Bi-fidelity variational auto-encoder for uncertainty quantification*, Computer Methods in Applied Mechanics and Engineering, 421 (2024), p. 116793.
 - [14] T. CUI, Y. MARZOUK, AND K. WILLCOX, *Scalable posterior approximations for large-scale bayesian inverse problems via likelihood-informed parameter and state reduction*, Journal of Computational Physics, 315 (2016), pp. 363–387.
 - [15] T. CUI, Y. M. MARZOUK, AND K. E. WILLCOX, *Data-driven model reduction for the bayesian solution of inverse problems*, International Journal for Numerical Methods in Engineering, 102 (2015), pp. 966–990.
 - [16] D. DEL-CASTILLO-NEGRETE, M. YANG, M. BEIDLER, AND G. ZHANG, *Generation and mitigation of runaway electrons: spatio-temporal effects in dynamic scenarios*, tech. report, Oak Ridge National Laboratory (ORNL), Oak Ridge, TN (United States), 2021.
 - [17] P. DHARIWAL AND A. NICHOL, *Diffusion models beat gans on image synthesis*, Advances in neural information processing systems, 34 (2021), pp. 8780–8794.
 - [18] O. R. DUNBAR, A. GARBUNO-INIGO, T. SCHNEIDER, AND A. M. STUART, *Calibration and uncertainty quantification of convective parameters in an idealized gcm*, Journal of Advances in Modeling Earth Systems, 13 (2021), p. e2020MS002454.
 - [19] Y. EFENDIEV, T. HOU, AND W. LUO, *Preconditioning markov chain monte carlo simulations using coarse-scale models*, SIAM Journal on Scientific Computing, 28 (2006), pp. 776–803.
 - [20] O. EMBRÉUS, A. STAHL, AND T. FÜLÖP, *On the relativistic large-angle electron collision operator for runaway avalanches in plasmas*, Journal of Plasma Physics, 84 (2018), p. 905840102.
 - [21] M. FAN, Z. ZHANG, D. LU, AND G. ZHANG, *Genai4uq: A software for inverse uncertainty quantification using conditional generative models*, arXiv preprint arXiv:2412.07026, (2024).
 - [22] N. GENEVA AND N. ZABARAS, *Multi-fidelity generative deep learning turbulent flows*, arXiv preprint arXiv:2006.04731, (2020).
 - [23] M. B. GILES, *Multilevel monte carlo methods*, Acta numerica, 24 (2015), pp. 259–328.
 - [24] I. GOODFELLOW, J. POUGET-ABADIE, M. MIRZA, B. XU, D. WARDE-FARLEY, S. OZAIR, A. COURVILLE, AND Y. BENGIO, *Generative adversarial nets*, Advances in neural information processing systems, 27 (2014).
 - [25] W. K. HASTINGS, *Monte carlo sampling methods using markov chains and their applications*, (1970).
 - [26] L. HESSLOW, O. EMBRÉUS, M. HOPPE, T. DUBOIS, G. PAPP, M. RAHM, AND T. FÜLÖP, *Generalized collision operator for fast electrons interacting with partially ionized impurities*, Journal of Plasma Physics, 84 (2018), p. 905840605.
 - [27] L. HESSLOW, O. EMBRÉUS, A. STAHL, T. C. DUBOIS, G. PAPP, S. L. NEWTON, AND T. FÜLÖP,

- Effect of partially screened nuclei on fast-electron dynamics*, Physical review letters, 118 (2017), p. 255001.
- [28] D. HIGDON, H. LEE, AND Z. BI, *A bayesian approach to characterizing uncertainty in inverse problems using coarse and fine-scale information*, IEEE Transactions on Signal Processing, 50 (2002), pp. 389–399.
- [29] J. HO, A. JAIN, AND P. ABBEEL, *Denoising diffusion probabilistic models*, Advances in neural information processing systems, 33 (2020), pp. 6840–6851.
- [30] E. HOOGEBOOM, D. NIELSEN, P. JAINI, P. FORRÉ, AND M. WELLING, *Argmax flows and multinomial diffusion: Learning categorical distributions*, Advances in Neural Information Processing Systems, 34 (2021), pp. 12454–12465.
- [31] A. KHORASHADIZADEH, K. KOTHARI, L. SALSU, A. A. HARANDI, M. DE HOOP, AND I. DOKMANIĆ, *Conditional injective flows for bayesian imaging*, IEEE Transactions on Computational Imaging, 9 (2023), pp. 224–237.
- [32] D. P. KINGMA, *Auto-encoding variational bayes*, arXiv preprint arXiv:1312.6114, (2013).
- [33] C. LI, J. LI, G. WANG, AND L. CARIN, *Learning to sample with adversarially learned likelihood-ratio*, (2018).
- [34] F. LI AND Y. MARZOUK, *Diffusion map particle systems for generative modeling*, arXiv preprint arXiv:2304.00200, (2023).
- [35] Y. LIU, Y. CHEN, D. XIU, AND G. ZHANG, *A training-free conditional diffusion model for learning stochastic dynamical systems*, arXiv preprint arXiv:2410.03108, (2024).
- [36] Y. LIU, M. YANG, Z. ZHANG, F. BAO, Y. CAO, AND G. ZHANG, *Diffusion-model-assisted supervised learning of generative models for density estimation*, Journal of Machine Learning for Modeling and Computing, 5 (2024).
- [37] D. LU, Y. LIU, Z. ZHANG, F. BAO, AND G. ZHANG, *A diffusion-based uncertainty quantification method to advance e3sm land model calibration*, Journal of Geophysical Research: Machine Learning and Computation, 1 (2024), p. e2024JH000234.
- [38] D. LU, D. M. RICCIUTO, AND J. ZHANG, *Invertible neural networks for e3sm land model calibration and simulation*, tech. report, Oak Ridge National Lab.(ORNL), Oak Ridge, TN (United States), 2022.
- [39] X. MA, C. ZHOU, X. LI, G. NEUBIG, AND E. HOVY, *Flowseq: Non-autoregressive conditional sequence generation with generative flow*, arXiv preprint arXiv:1909.02480, (2019).
- [40] D. MAOUTSA, S. REICH, AND M. OPPER, *Interacting particle solutions of fokker–planck equations through gradient–log–density estimation*, Entropy, 22 (2020), p. 802.
- [41] C. J. MCDEVITT, Z. GUO, AND X.-Z. TANG, *Avalanche mechanism for runaway electron amplification in a tokamak plasma*, Plasma Physics and Controlled Fusion, 61 (2019), p. 054008.
- [42] N. MIMIKOS-STAMATOPOULOS, B. J. ZHANG, AND M. A. KATSOULAKIS, *Score-based generative models are provably robust: an uncertainty quantification perspective*, arXiv preprint arXiv:2405.15754, (2024).
- [43] G. PAPAMAKARIOS, E. NALISNICK, D. J. REZENDE, S. MOHAMED, AND B. LAKSHMINARAYANAN, *Normalizing flows for probabilistic modeling and inference*, The Journal of Machine Learning Research, 22 (2021), pp. 2617–2680.
- [44] D. V. PATEL AND A. A. OBERAI, *Gan-based priors for quantifying uncertainty in supervised learning*, SIAM/ASA Journal on Uncertainty Quantification, 9 (2021), pp. 1314–1343.
- [45] B. PEHERSTORFER, T. CUI, Y. MARZOUK, AND K. WILLCOX, *Multifidelity importance sampling*, Computer Methods in Applied Mechanics and Engineering, 300 (2016), pp. 490–509.
- [46] B. PEHERSTORFER, K. WILLCOX, AND M. GUNZBURGER, *Optimal model management for multifidelity monte carlo estimation*, SIAM Journal on Scientific Computing, 38 (2016), pp. A3163–A3194.
- [47] B. PEHERSTORFER, K. WILLCOX, AND M. GUNZBURGER, *Survey of multifidelity methods in uncertainty propagation, inference, and optimization*, Siam Review, 60 (2018), pp. 550–591.
- [48] P. PERDIKARIS, M. RAISSI, A. DAMIANOU, N. D. LAWRENCE, AND G. E. KARNIADAKIS, *Nonlinear information fusion algorithms for data-efficient multi-fidelity modelling*, Proceedings of the Royal Society A: Mathematical, Physical and Engineering Sciences, 473 (2017), p. 20160751.
- [49] X. QIAO, W. LI, B. XIAO, Y. HUANG, AND L. YANG, *Score-based generative priors guided model-driven network for mri reconstruction*, arXiv preprint arXiv:2405.02958, (2024).
- [50] T. SALIMANS, I. GOODFELLOW, W. ZAREMBA, V. CHEUNG, A. RADFORD, AND X. CHEN, *Improved techniques for training gans*, Advances in neural information processing systems, 29 (2016).
- [51] T. SCHLEGL, P. SEEBÖCK, S. M. WALDSTEIN, U. SCHMIDT-ERFURTH, AND G. LANGS, *Unsupervised anomaly detection with generative adversarial networks to guide marker discovery*,

- in International conference on information processing in medical imaging, Springer, 2017, pp. 146–157.
- [52] D. SHIRAKI, N. COMMAUX, L. BAYLOR, C. COOPER, N. EIDIETIS, E. HOLLMANN, C. PAZ-SOLDAN, S. COMBS, AND S. MEITNER, *Dissipation of post-disruption runaway electron plateaus by shattered pellet injection in dIII-d*, Nuclear Fusion, 58 (2018), p. 056006.
- [53] S. A. SISSON, Y. FAN, AND M. BEAUMONT, *Handbook of approximate Bayesian computation*, CRC press, 2018.
- [54] Y. SONG AND S. ERMON, *Generative modeling by estimating gradients of the data distribution*, Advances in neural information processing systems, 32 (2019).
- [55] Y. SONG, J. SOHL-DICKSTEIN, D. P. KINGMA, A. KUMAR, S. ERMON, AND B. POOLE, *Score-based generative modeling through stochastic differential equations*, arXiv preprint arXiv:2011.13456, (2020).
- [56] Y. SUN, Z. WU, Y. CHEN, B. T. FENG, AND K. L. BOUMAN, *Provable probabilistic imaging using score-based generative priors*, IEEE Transactions on Computational Imaging, (2024).
- [57] Z. O. WANG, R. BAPTISTA, Y. MARZOUK, L. RUTHOTTO, AND D. VERMA, *Efficient neural network approaches for conditional optimal transport with applications in bayesian inference*, arXiv preprint arXiv:2310.16975, (2023).
- [58] T. WEBER, A. COROTAN, B. HUTCHINSON, B. KRAVITZ, AND R. LINK, *Deep learning for creating surrogate models of precipitation in earth system models*, Atmospheric Chemistry and Physics, 20 (2020), pp. 2303–2317.
- [59] M. XI, D. LU, D. GUI, Z. QI, AND G. ZHANG, *Calibration of an agricultural-hydrological model (rzwqm2) using surrogate global optimization*, Journal of Hydrology, 544 (2017), pp. 456–466.
- [60] D. XIU AND G. KARNIADAKIS, *Supersensitivity due to uncertain boundary conditions*, Int. J. Numer. Meth. Engng., 61 (2004), pp. 2114–2138.
- [61] Z. XU, Y. CHEN, Q. CHEN, AND D. XIU, *Modeling unknown stochastic dynamical system via autoencoder*, Journal of Machine Learning for Modeling and Computing, 5 (2024).
- [62] M. YANG, P. WANG, D. DEL CASTILLO-NEGRETE, Y. CAO, AND G. ZHANG, *A pseudoreversible normalizing flow for stochastic dynamical systems with various initial distributions*, SIAM Journal on Scientific Computing, 46 (2024), pp. C508–C533.
- [63] Y. YANG AND P. PERDIKARIS, *Adversarial uncertainty quantification in physics-informed neural networks*, Journal of Computational Physics, 394 (2019), pp. 136–152.
- [64] A. ZAMMIT-MANGION, M. SAINSBURY-DALE, AND R. HUSER, *Neural methods for amortized inference*, Annual Review of Statistics and Its Application, 12 (2024).